



**HAL**  
open science

# Time-dependent ab initio approaches for high-harmonic generation spectroscopy

Emanuele Coccia, Eleonora Luppi

► **To cite this version:**

Emanuele Coccia, Eleonora Luppi. Time-dependent ab initio approaches for high-harmonic generation spectroscopy. *Journal of Physics: Condensed Matter*, 2021, 34 (7), pp.073001. 10.1088/1361-648X/ac3608 . hal-04023377

**HAL Id: hal-04023377**

**<https://hal.science/hal-04023377>**

Submitted on 10 Mar 2023

**HAL** is a multi-disciplinary open access archive for the deposit and dissemination of scientific research documents, whether they are published or not. The documents may come from teaching and research institutions in France or abroad, or from public or private research centers.

L'archive ouverte pluridisciplinaire **HAL**, est destinée au dépôt et à la diffusion de documents scientifiques de niveau recherche, publiés ou non, émanant des établissements d'enseignement et de recherche français ou étrangers, des laboratoires publics ou privés.

## TOPICAL REVIEW

# Time-dependent ab initio approaches for high-harmonic generation spectroscopy

**Emanuele Coccia**

Dipartimento di Scienze Chimiche e Farmaceutiche, via Giorgieri 1, 34127 Trieste, Italy

E-mail: [ecoccia@units.it](mailto:ecoccia@units.it)

**Eleonora Luppi**

Sorbonne Universités, UPMC Univ Paris 06, UMR 7616, Laboratoire de Chimie Théorique, F-75005 Paris, France.  
CNRS, UMR 7616, Laboratoire de Chimie Théorique, F-75005 Paris, France

E-mail: [eleonora.luppi@upmc.fr](mailto:eleonora.luppi@upmc.fr)

### **Abstract.**

High-harmonic generation (HHG) is a nonlinear physical process used for the production of ultrashort pulses in XUV region, which are then used for investigating ultrafast phenomena in time-resolved spectroscopies. Moreover, HHG signal itself encodes information on electronic structure and dynamics of the target, possibly coupled to nuclear degrees of freedom. Investigating HHG signal leads to HHG spectroscopy, which is applied to atoms, molecules, solids and recently also to liquids. Analysing the number of generated harmonics, their intensity and shape gives a detailed insight of, e.g., ionisation and recombination channels occurring in the strong-field dynamics. A number of valuable theoretical models has been developed over the years to explain and interpret HHG features, with the three-step model being the most known one. Originally, these models neglect the complexity of the propagating electronic wavefunction, by only using an approximated formulation of ground and continuum states. Many effects unravelled by HHG spectroscopy are instead due to electron correlation effects, quantum interference, and Rydberg-state contributions, which are all properly captured by an ab initio electronic-structure approach. In this Review we have collected recent advances in modelling HHG by means of ab initio time-dependent approaches relying on the propagation of the time-dependent Schrödinger equation (or derived equations) in presence of a very intense electromagnetic field. We limit ourselves to gas-phase atomic and molecular targets, and to solids. We focus on the various levels of theory for describing the electronic structure of the target, coupled with strong-field dynamics and ionisation approaches, and on the basis used to represent electronic states. Selected applications and perspectives for future developments are also given.

## 1. Introduction

High-harmonic generation (HHG) was observed for the first time in 1977 in CO<sub>2</sub> laser interaction with plasmas generated from solid Al targets [1]. Instead, HHG in gases was first observed in 1987 [2, 3]. HHG spectrum covers a very broad spectral range, from visible light to soft X-rays, and has a distinctive shape: a rapid decrease of the intensity for the low-order harmonics consistent with perturbation theory, followed by a broad plateau region where the harmonic intensity remains almost constant, and then an abrupt cutoff, beyond which almost no harmonics are observed.

The physical mechanism behind the harmonics generation was understood by a semi-classically model (3SM) as a sequence of three steps [4, 5]: (i) an electron escapes from the nucleus (or nuclei) through tunnel ionisation associated with the strong laser field, (ii) the electron is then accelerated away by the laser field until the sign of the field changes, (iii) whereupon the electron is reaccelerated back to the nucleus (or nuclei), with the system emitting a photon as the electron recombines to the parent ion. A key quantity emerging from the model is the maximum energy the field can provide to the electron,  $E_{\text{cutoff}} = I_p + 3.17U_p$ , where  $I_p$  is the ionisation potential and  $U_p = E_0^2/(4\omega_0)^2$  is the ponderomotive energy where  $E_0$  is the maximum amplitude of the pulse and  $\omega_0$  is the carrier frequency. In this model the cutoff scales linearly with  $E_0^2$ . [4, 5]

In 2001 the first experimental demonstration of attosecond ( $10^{-18}$  s) pulses via HHG was obtained. [6] Since then impressive advances in laser technology were developed, introducing new time-resolved spectroscopies which offer the opportunity to investigate electron dynamics with unprecedented time resolution [7–19].

Dynamical and structural information can be extracted from HHG spectra associated with the attosecond dynamics, shedding light on laser- and correlation-driven effects in strong-field dynamics. For instance in the study of different ionisation and recombination channels, [11, 20–23] molecular imaging [24–28] ultrafast charge migration [29], vibrational signatures [30], quantum coherence in atoms [31] and electron dynamics of organic molecules and biomolecules [18, 32–37].

In 2011, HHG from solids was measured for the first time [38]. The generation mechanism of HHG in solids involves inter- and intraband electronic dynamics and also in this case a semiclassical 3SM was proposed: (i) an electron tunnels from the valence to the conduction band and (ii) it is accelerated in the conduction band while its hole is accelerated in the valence band, which will lead to an intraband current, and (iii) then the electron and the hole recombine giving rise to an interband polarisation. With respect to atoms and molecules, HHG in solids has a quite different behaviour, starting from a different cutoff law which scales linearly with  $E_0$  and which is limited to the energy band gap of the solid [38–40]. Moreover, as the electron density in solids is higher than in gases the harmonic yield is expected to be higher.

HHG in solids offers a unique and attracting way to probe electron dynamics in solids at attosecond timescale. Moreover, HHG can be achieved in a wide range of solid materials, from semiconductors to novel two-dimensional materials. [41–50] HHG in solids also represents an attractive route towards compact table-top light-source for coherent and bright attosecond pulses in the extreme ultraviolet and soft x-ray energy regime. [51–54]

Despite these exciting experimental achievements, reaching a clear understanding of the mechanisms that control the electron dynamics under the action of a strong laser field is still challenging, which necessarily requires theoretical support. Developing theoretical and computational methods able to provide an accurate treatment of the fundamental processes generated by an intense laser field is therefore crucial.

The proper treatment of the time-dependent electronic wavefunction, and therefore of the many-electron dynamics, under the influence of an intense pulse is obtained by propagating the time-dependent Schrödinger equation (TDSE). The electron dynamics implicated in the HHG process can be rather complex [29, 32, 55–59]. Indeed, when the laser interacts with the system a non-stationary electronic wavefunction, consisting of a coherent superposition of excited states, is generated. The time evolution of the wavefunction involves changing interference and coupling between the different excited states, including Rydberg and continuum states. Moreover, the wavefunction dynamics is determined by parameters of the laser such as intensity, duration, polarisation, phase and carrier frequency.

Approximated theoretical methods have been developed to study HHG in atoms, molecules and solids. For atoms and molecules the time-dependent Schrödinger equation (TDSE) was solved within the single-active electron (SAE) in the strong-field approximation (SFA). [60–64] For solids, numerical methods related to TDSE have also been developed, together with the use of the semiconductor Bloch equations.[65]

Concerning ab initio methods, nowadays, the electron-dynamics problem in strong fields is tackled by two main families of time-dependent electronic-structure approaches [66]: real time time-dependent density-functional theory (RT-TDDFT) [67–86] and real-time time-dependent wavefunction methods (RT-TDWF)[87–97]. The many-electron dynamics is described in RT-TDDFT by the time-dependent density [98, 99] and in RT-TDWF by a (correlated) time-dependent wavefunction. Despite the different theoretical principles, RT-TDDFT and RT-TDWF share some theoretical and computational aspects concerning the strategy used to propagate the TDSE. Time propagation is directly applied to the molecular orbitals (MOs) [75, 80–82] or to a truncated basis composed of the ground- and excited-state wavefunctions of the field-free electronic Hamiltonian [67, 68, 70, 100–102].

Theoretical methods developed in the framework of RT-TDDFT and RT-TDWF describe the electron correlation within different levels of accuracy. In RT-TDDFT the many-electron effects are encoded in the time-dependent exchange-correlation potential  $v_{xc}$  or in the exchange-correlation kernel  $f_{xc}$ . These are complicated quantities as they are nonlocal in time and space, and need to fulfil specific mathematical behaviour in order to accurately describe the strong-field electron dynamics [103–111]. Instead, in RT-TDWF many-electron features in HHG are described through the complexity of the time-dependent wavefunction obtained from the time-dependent extension of well-established methods [112] such as configuration interaction (CI), coupled cluster (CC) and multiconfigurational self-consistent field (MCSCF) [75, 76, 80, 84, 113–115].

Other than RT-TDDFT and RT-TDWF developments on the accurate description of electron correlation, another essential aspect needs to be carefully addressed from theory, because of the high energies involved in the HHG nonlinear response: the choice of the one-electron basis for representing the time-dependent wavefunction. In fact, a reliable description of the electron dynamics in strong laser fields depends on the accuracy in reproducing both the bound and the continuum states, which are appreciably populated during the dynamics, of the molecular system considered [68]. In addition, choosing a good basis can improve the numerical convergence of the results and reduce the computational cost of simulations.

In this review we focus on RT-TDWF and RT-TDDFT methods for the description of HHG in atoms, molecules and solids. We review theory in Section 2, in detail: TDSE in Section 2.1; RT-TDWF and RT-TDDFT methods are described in Section 2.2 and 2.3; options for a proper basis for the wavefunction representation in HHG are given in Section 2.4; selected applications to HHG spectroscopy are reported in Section 3; conclusions and perspectives for future works are then proposed in the last Section. Hartree atomic units are used throughout the text.

## 2. Theory

Approaches collected in this Section are general and in principle applicable to any kind of system. In practice, only RT-TDDFT by propagating Kohn-Sham (KS) orbitals is used to compute HHG spectra of solids, as will be shown in Section 3.

### 2.1. Time-dependent Schrödinger equation

The dynamics of  $N$  interacting electrons in an external electric field is described by the TDSE

$$i\frac{d|\Psi(t)\rangle}{dt} = \hat{H}(t)|\Psi(t)\rangle, \quad (1)$$

together with the initial condition  $|\Psi(t_0)\rangle = |\Psi_0\rangle$ , where  $t_0$  and  $|\Psi_0\rangle$  are the initial propagation time and the starting wavefunction, typically the electronic ground state.

The time-dependent Hamiltonian is defined as

$$\hat{H}(t) = \hat{T} + \hat{W}_{ee} + \hat{V}_{ne} + \hat{V}_{\text{ext}}(t), \quad (2)$$

where the kinetic operator is  $\hat{T} = -\frac{1}{2} \int [\nabla_{\mathbf{r}}^2 \hat{n}_1(\mathbf{r}, \mathbf{r}')]_{\mathbf{r}'=\mathbf{r}} d\mathbf{r}$ , the electron-electron Coulomb interaction is  $\hat{W}_{ee} = \frac{1}{2} \iint \hat{n}_2(\mathbf{r}, \mathbf{r}') w_{ee}(|\mathbf{r} - \mathbf{r}'|) d\mathbf{r} d\mathbf{r}'$ , the electron-nuclei Coulomb interaction is  $\hat{V}_{ne} = \int \hat{n}(\mathbf{r}) v_{ne}(\mathbf{r}) d\mathbf{r}$  and the external-field perturbation is  $\hat{V}_{\text{ext}}(t)$ .  $\mathbf{r}$  ( $\mathbf{r}'$ ) represents the electronic coordinates. The external-field perturbation in the length gauge is  $\hat{V}_{\text{ext}}(t) = -\hat{\boldsymbol{\mu}} \cdot \mathbf{E}(t)$  where  $\hat{\boldsymbol{\mu}}$  is the dipole operator and  $\mathbf{E}(t)$  is the external electric field, while in the velocity gauge  $\hat{V}_{\text{ext}}(t) = -\hat{\mathbf{A}}(t) \cdot \hat{\mathbf{p}}$ , where  $\hat{\mathbf{p}}$  is the momentum operator and  $\mathbf{A}(t)$  is the vector potential [61, 116]. In these definitions,  $\hat{n}_1(\mathbf{r}, \mathbf{r}')$  is the one-particle density operator,  $\hat{n}_2(\mathbf{r}, \mathbf{r}')$  is the pair-density operator,  $\hat{n}(\mathbf{r})$  is the density operator,  $w_{ee}(|\mathbf{r} - \mathbf{r}'|)$  is the two-electron repulsion potential term, and  $v_{ne}(\mathbf{r})$  is the electron-nucleus attraction potential term. A classical description of the external electric field is taken into account in this work, while a fully quantum description of HHG nonlinear optics is found in Ref. [117].

The HHG spectrum is then computed as the power spectrum  $P_{\xi}(\omega)$

$$P_{\xi}(\omega) = \left| \frac{1}{t_f - t_i} \int_{t_i}^{t_f} \langle \Psi(t) | \hat{\xi} \cdot \hat{\mathbf{n}} | \Psi(t) \rangle e^{-i\omega t} dt \right|^2, \quad (3)$$

where the operator  $\hat{\xi}$  can be either equal to the electron-dipole operator  $\hat{\boldsymbol{\mu}}$ , or to the electron-velocity operator  $\hat{\mathbf{v}} = -i [\hat{\boldsymbol{\mu}}, \hat{H}(t)]$  or to the electron-acceleration operator  $\hat{\mathbf{a}} = -i [\hat{\mathbf{v}}, \hat{H}(t)]$  [70, 118] and  $\hat{\mathbf{n}}$  is the unit vector in the polarization direction.  $t_i$  and  $t_f$  are initial and final times for Fourier transform, respectively:  $t_0$  for the initial condition of Eq. 1 and  $t_i$  in Eq. 3 do not necessarily coincide.

In solids, the power spectrum is written in terms of the current as [47, 119]

$$P_j(\omega) = \left| \frac{1}{t_f - t_i} \int_{t_i}^{t_f} \frac{\partial}{\partial t} \mathbf{J}(t) \cdot \hat{\mathbf{n}} e^{-i\omega t} dt \right|^2. \quad (4)$$

where  $\mathbf{J}(t)$  is the time-dependent induced current.

However, the TDSE cannot be solved exactly in most of the systems because of the high dimensionality of the electron-electron interaction. Therefore, different RT-TDWF and RT-TDDFT methodologies have been developed to approximate its solution or to provide a valid alternative to TDSE, as reviewed in Sections 2.2 and 2.3.

## 2.2. Time-dependent methods

Time-domain extension of configuration interaction [112] (TD-CI), multiconfigurational (MC) methods [112] (MCTDHF and TD-MCSCF), coupled cluster [112] (TC-CC) and algebraic diagrammatic construction [120, 121] (TD-ADC) is reported in this Section. These RT-TDWF methods have been applied to interpret, predict and explain HHG features in atoms and molecules, as shown in Section 3.

*2.2.1. TD-CI methods* In TD-CI the time-dependent wavefunction is defined as

$$|\Psi(t)\rangle = \sum_k c_k(t) |\Psi_k\rangle, \quad (5)$$

where  $c_k(t)$  are time-dependent coefficients and  $|\Psi_k\rangle = \hat{R}_k |\Phi_0\rangle$  are CI eigenfunctions written in terms of the excitation operator  $\hat{R}_k = r_{0,k} + \sum_{ia} r_{i,k}^a \hat{a}_a^\dagger \hat{a}_i + \sum_{ijab} r_{ij,k}^{ab} \hat{a}_a^\dagger \hat{a}_b^\dagger \hat{a}_i \hat{a}_j + \dots$  and of the ground-state Slater determinant of MOs  $|\phi_p\rangle$ , which is  $|\Phi_0\rangle = |\phi_1 \dots \phi_N\rangle$ . The index  $k = 0$  corresponds to the ground-state eigenfunction and  $k = 1, \dots, N$  to the excited-state ones. The indices  $i, j, k$ , etc. are for occupied orbitals,  $a, b, c$ , etc. are for virtual orbitals, and  $p, q, r$ , etc. for generic orbitals. The operators  $\hat{a}_p^\dagger$  and  $\hat{a}_p$  create and annihilate an electron from the orbital  $|\phi_p\rangle$ , and the amplitudes,  $r_{0,k}, r_{i,k}^a, r_{ij,k}^{ab} \dots$  are determined by minimising the total CI energy [113].

This approach is typically used by limiting the excited-state manifold to only singly-excited configurations (TD-CIS), singly-excited and perturbative double-excited configurations (TD-CIS(D)), or full singly- and doubly-excited ones (TD-CISD). In TD-CIS the Slater determinant  $|\Phi_0\rangle$  is the Hartree-Fock (HF) ground state, while for TD-CIS(D) and TD-CISD is the perturbative MP2 [112] ground state [67, 69–71, 80, 101, 111, 122–125]. In most electron-dynamics applications, HHG included, TD-CIS is considered as a reasonable compromise between accuracy and computational effort [126].

Another version of the TD-CI method explicitly includes the time-dependence in the excitation operator as

$$\hat{R}_k(t) = r_{0,k}(t) + \sum_{ia} r_{i,k}^a(t) \hat{a}_a^\dagger \hat{a}_i + \sum_{ijab} r_{ij,k}^{ab}(t) \hat{a}_a^\dagger \hat{a}_b^\dagger \hat{a}_i \hat{a}_j + \dots \quad (6)$$

from which the time-dependent wave function is

$$|\Psi(t)\rangle = \hat{R}_k(t) |\Phi_0\rangle. \quad (7)$$

This approach was used for HHG in TD-CIS framework [83, 85, 116, 127–130].

In both cases of Eqs 5 and 7 the time-dependent  $|\Psi(t)\rangle$  is propagated according to Eq. 1 and then used to compute the HHG spectrum by means of Eq. 3.

*2.2.2. MCTDHF and TD-MCSCF methods* The time-dependent wavefunction in MCTDHF is a full CI expansion defined as

$$|\Psi(t)\rangle = \sum_k c_k(t) |\Phi_k(t)\rangle, \quad (8)$$

where both  $c_k(t)$  expansion coefficients and MOs, i.e.  $|\phi_p(t)\rangle$ , defining the Slater determinants  $|\Phi_k(t)\rangle$ , are time-dependent [131–135]. The use of time-dependent MOs implies more flexibility compared to the methods described in Section 2.2.1. Since the MCTDHF computational cost becomes prohibitive for many-electron dynamics, several approximations have been developed. Indeed, truncating of the CI expansion in MCTDHF reduces to the TD-MCSCF, where only a small number of MOs is used. In turn, the introduction of frozen-core, dynamical-core, and active orbital subspaces bring to the TD-CASSCF method [136]. An even more flexible classification of the active-orbital subspace is given by other methods such as the time-dependent restricted-active-space self-consistent field (TD-RASSCF) and time-dependent occupation-restricted multiple-active-space (TD-ORMAS)[75, 76, 79, 136–138].

*2.2.3. Time-dependent Coupled Cluster* The TD-CC method uses a nonHermitian Hamiltonian  $\hat{H}$  which depends on the cluster operator

$$\hat{T}_{\text{CC}} = \sum_{ia} t_i^a \hat{a}_a^\dagger \hat{a}_i + \frac{1}{4} \sum_{ijab} t_{ij}^{ab} \hat{a}_a^\dagger \hat{a}_b^\dagger \hat{a}_i \hat{a}_j + \dots, \quad (9)$$

with not necessarily real eigenvalues, and with distinct left and right eigenvectors for each eigenvalue.  $t_i^a$ ,  $t_{ij}^{ab}$  are amplitudes related to the usual single, double,... excitations. As a consequence of the nonHermitian nature of the approach, TD-CC is characterised by right (R) time-dependent wavefunctions

$$|\Psi^R(t)\rangle = \sum_k c_k^R(t) \hat{R}_k |\Phi_0\rangle, \quad (10)$$

and by left (L) time-dependent wavefunctions

$$\langle \Psi^L(t) | = \sum_k \langle \Phi_0 | \hat{L}_k c_k^L(t), \quad (11)$$

where  $\hat{L}_k$  has the same form as the excitation operator  $\hat{R}_k$  in Section 2.2.1. Within this approach HHG spectra have been calculated using a time-dependent dipole moment where the nonHermitian component has been dropped [67].

Similarly with what has been described in Section 2.2.1 for TD-CI, a different TD-CC formulation is based on the definition of of an explicit time-dependent cluster operator [81]

$$\hat{T}_{\text{CC}}(t) = \sum_{ia} t_i^a(t) \hat{a}_a^\dagger \hat{a}_i + \frac{1}{4} \sum_{ijab} t_{ij}^{ab}(t) \hat{a}_a^\dagger \hat{a}_b^\dagger \hat{a}_i \hat{a}_j + \dots \quad (12)$$

from which the time-dependent wavefunction is given by

$$|\Psi(t)\rangle = e^{\hat{T}_{\text{CC}}(t)} |\Phi_0\rangle. \quad (13)$$

The inclusion of the time-dependence also in the MOs of  $|\Phi_0\rangle$  is developed in the time-dependent optimised coupled-cluster (TD-OCC) method [114]. This method was implemented including double excitations (TD-OCCD) and double and triple excitations (TD-OCCDT). In the framework of the TD-OCC, TD-OCEPA0 [115] and TD-OMP2 [139] methods have been used for the calculation of HHG spectra.

*2.2.4. Time-dependent ADC* The time-dependent wavefunction in TD-ADC is

$$|\Psi(t)\rangle = \sum_k c_k(t) |\tilde{\Psi}_k\rangle, \quad (14)$$

where  $c_k(t)$  are time-dependent coefficients and  $|\tilde{\Psi}_k\rangle$  are the ADC intermediate states obtained from the correlated excited states  $|\Psi_k\rangle = \hat{C}_k^\dagger |\Psi_0\rangle$  where  $\hat{C}_k^\dagger = \{\hat{a}_a^\dagger \hat{a}_i, \hat{a}_a^\dagger \hat{a}_b^\dagger \hat{a}_i \hat{a}_j, \dots\}$  and  $|\Psi_0\rangle$  is the exact ground state.

In the ADC hierarchy the first-order ADC(1) method, which is considered as an improved version of CIS [73, 140], has been used for HHG spectroscopy [73, 140].

### 2.3. Time-dependent density-functional theory

The foundation of TDDFT is the Runge-Gross theorem [98], which states that the properties of the interacting-electron system can be calculated from the knowledge of the time-dependent density  $n(\mathbf{r}, t)$  with a fixed initial condition.  $n(\mathbf{r}, t)$  is accessible from the time-dependent KS scheme which replaces the interacting system by a non-interacting one with the same time-dependent density [141].

The time-dependent KS equations are

$$i \frac{d|\varphi_i(t)\rangle}{dt} = \left[ \hat{T} + \hat{V}_{\text{ks}}[n](t) \right] |\varphi_i(t)\rangle, \quad (15)$$

where  $|\varphi_i(t)\rangle$  are the time-dependent KS MOs,  $\hat{V}_{\text{ks}}[n](t)$  is the sum of  $\hat{V}_{\text{ext}}(t)$ , the Hartree potential operator  $\hat{V}_{\text{H}}[n](t) = \int \hat{n}(\mathbf{r}) v_{\text{H}}[n](\mathbf{r}, t) d\mathbf{r}$  and the exchange-correlation potential operator  $\hat{V}_{\text{xc}}[n](t) = \int \hat{n}(\mathbf{r}) v_{\text{xc}}[n](\mathbf{r}, t) d\mathbf{r}$ , which has to be approximated. Once Eq. (15) is solved the exact density is straightforwardly calculated as  $n(\mathbf{r}, t) = \sum_i |\varphi_i(\mathbf{r}, t)|^2$ . The time-dependent wavefunction is a single Slater determinant constructed from the time-dependent KS orbitals  $|\varphi_i\rangle$  of Eq. (15). In the case of solids, propagation of KS equations within the TDDFT is coupled to Maxwell equations for the electromagnetic fields [41, 142] to account for macroscopic propagation effects in the material.

The many-electron effects are encoded in the time-dependent exchange-correlation potential  $v_{xc}$ , which is a functional of the density, and also, in principle, depends on all previous times. However, in most of the cases, the adiabatic approximation is used, i.e.  $v_{xc}$  is evaluated at the instantaneous time-dependent density [143]. However, known artefacts from time-dependent KS equations in describing the response to light pulses and Rabi oscillations are attributed to the adiabatic approximation [144–146].

Correctly reproducing the long-range behaviour of  $v_{xc}$  is necessary to accurately describe the strong-field electron dynamics in RT-TDDFT. This permits to properly estimate the ionisation threshold energy, giving the onset of the continuum spectrum. Different strategies have been introduced such as self-interaction corrections (SIC) [103, 104], range-separated functionals [105–108] and long-range corrected potentials [109].

Instead, the RT-TDDFT approaches that propagate a truncated eigenstate basis, constructed from linear-response TDDFT [147, 148], describe the many-electron effects through the exchange-correlation kernel  $f_{xc}$ . The  $f_{xc}$  is the functional derivative of  $v_{xc}$  with respect to the density and also needs to be approximated.  $f_{xc}$  is nonlocal in time and space, but the most common approximations are adiabatic and only the nonlocality in space is taken into account. It is worth mentioning that using TDSE with a basis given by TDDFT pseudo wavefunctions in linear response overcomes the difficulty to have a time-dependent xc kernel, provided an accurate representation of electronic excitations.

Within this approach as well, including long-range effects for the  $f_{xc}$  is an important task. Range-separated approaches are among the most successful schemes to model the space dependence. Usually, in these approaches, the exchange part of the  $f_{xc}$ , i.e.  $f_x$ , is decomposed in a long-range (lr) HF and a short-range (sr) DFT component:  $f_x = f_{x, \text{HF}}^{\text{lr}} + f_x^{\text{sr}}$  [108, 110, 111].

#### 2.4. Basis representation

In presence of a strong field, all the above described RT-TDWF and RT-TDDFT methods require special care about the basis-set representation of the time-dependent wavefunction. As exemplified by the 3SM, during HHG an electron is liberated in the continuum where it behaves as a (nearly) free charged particle and it is then reaccelerated back to the parent ion. This implies that an adequate theoretical modelling must be able to represent bound states as well as high-energy oscillatory wavefunctions describing continuum states. This ability relies in the basis set used to describe the time-dependent wavefunction.

Spatial grid methods have been largely used to describe strong-field electron dynamics and HHG in atoms, molecules and solids [46, 47, 49, 50, 114, 128, 129, 142, 149–156]. A careful choice of the size and the discretisation of the grid box in connection to the pulse intensity, frequency and phase is required. Therefore, the computational cost can quickly increase and strategies involving multi-level parallelisation schemes have been developed [157–159].

B-splines [160] basis set approaches are competitive with spatial grid methods. B-splines are piecewise polynomial and  $L^2$ -integrable functions defined in a restricted sampled space. B-splines show smooth connections between the various pieces, making them highly flexible in fitting any type continuous curve. In fact, B-splines are able to provide a very accurate representation of continuum states and demonstrated to accurately describe dynamical strong-field properties of atoms and molecules [108, 161, 162].

Recently, Gaussian-type orbitals (GTOs) have been successfully used to compute HHG of atomic and molecular species [31, 67–71, 100–102, 111, 122–126, 147, 163–169]. GTOs are routinely used in quantum chemistry to compute bound-state properties [112]. Extension of GTOs to strong-field processes is extremely challenging, due to the intrinsic localised nature of Gaussian functions. Different strategies have been proposed to improve GTOs for the description of HHG, i.e. to provide a balanced basis set able to describe bound and continuum states with similar and reliable accuracy. In Ref. [163] GTOs are obtained by one-to-one fitting of a series of Slater-type orbitals (STOs) with fixed exponent and increasing principal quantum number (these GTOs are referred as K functions in this work). Linear combinations of GTOs have been generated by fitting spherical Bessel and Coulomb functions [164, 165]. Recently, a systematic construction of the GTO basis set has been proposed, based on the idea to optimise GTOs according to the states energetically accessible to the electron during the strong-field dynamics. Moreover, GTOs can also be placed in arbitrary points in space to improve description of the electronic density and of the liberated electron, by using the so called ghost atoms [69, 168].

Promising strategies for HHG are based on a hybrid basis, e.g. composed of GTO and B-splines [170, 171], GTO+grid representation [172] and plane-wave functions multiplied by the GTOs [166], or complex GTOs [173–176] and STOs [177–179].

Another important problem to be addressed is the incompleteness of any practically used basis set. In fact, regardless of the approach employed for the basis set (grid, B-splines, GTOs, ...), unphysical reflections of the electronic wavefunction must be avoided, which would lead to artificial features and high noise in HHG spectra. In HHG simulations two methods are typically exploited for accounting for the finite basis set: the complex absorbing potential (CAP) defined in real space [180–185], and the heuristic lifetime model [70, 71, 186] applied to electronic-state energies. Various forms of CAP have been proposed in literature, a typical one is a quadratic function of the electron

radial distance  $r$  [167]

$$V_{\text{CAP}}(r) = \eta \Theta(r - r_{\text{CAP}})(r - r_{\text{CAP}})^2, \quad (16)$$

where  $\Theta$  is the Heaviside function,  $\eta$  and  $r_{\text{CAP}}$  are two parameters defining the “strength” of absorption and the centre of CAP, respectively. Generalisation for nonspherical systems is also possible by including Euler angles.  $V_{\text{CAP}}$  is added in the time-dependent Hamiltonian as an imaginary term, i.e.  $iV_{\text{CAP}}$ . CAP approach is particularly suitable for grid-based representation of the electronic wavefunction, but it has been efficiently also implemented in GTO-based quantum-chemistry methods [185]. On the other hand, the heuristic lifetime model has been originally developed for GTO-based methods with a singly-excited ansatz [186]. The main idea behind this model, mainly applied to gas-phase targets, consists in interpreting the approximated field-free eigenstates above the ionization threshold as non-stationary states. In the time propagation this translates in replacing the energy  $E_k$  of the  $k$ -th excited state by complex energy  $E_k - \frac{i}{2}\Gamma_k$ , where  $\Gamma_k$  is the inverse lifetime of state  $k$ , defined as follows:

$$\Gamma_k = \begin{cases} 0 & \text{if } \omega_k < I_p \\ \sum_i \sum_a |r_{i,k}^a|^2 \frac{1}{d} \sqrt{\epsilon_a} & \text{if } \omega_k \geq I_p \text{ and } \epsilon_a > 0 \end{cases} \quad (17)$$

where  $|r_{i,k}^a|^2$  is the probability that an one-electron excitation from orbital  $i$  to orbital  $a$  takes place in the  $k$ -th excited state in a singly-excited ansatz, such as TD-CIS (Section 2.2.1), and  $d$  is an empirical parameter which represents the characteristic escape length that the electron in the state  $k$  is allowed to travel during the lifetime  $\frac{1}{\Gamma_k}$ .  $\omega_k$  and  $I_p$  are the excitation energy for the  $k$ -th state and the ionisation energy, respectively. The sum runs over all the occupied  $i$  and virtual  $a$  MOs. Evaluation of  $\Gamma_k$  is limited to virtual MOs with positive energy  $\epsilon_a$ . The factor  $-\frac{i}{2}\Gamma_k$  can be interpreted as an absorbing potential for state  $k$ , which is irreversibly depopulated by means of a lifetime  $\tau_k = \frac{1}{\Gamma_k}$ . As reported in Ref. [70], a slightly different approach consists in adopting two different values of the escape length  $d$ , named  $d_0$  and  $d_1$ : a large value of  $d_0$  (which corresponds to a small value of  $\Gamma_k$ ) needs to be used for all the above-ionisation threshold states with energy below the energy cutoff of the 3SM, while a smaller value for  $d_1$  translates into a larger  $\Gamma_n$  and is used for continuum states with energies above the 3SM cutoff energy. An ab initio derivation of the heuristic lifetime model was proposed in Ref. [71], together with the extension to the CISD ansatz, which also includes doubly-excited electronic configurations.

### 3. Applications

#### 3.1. Atoms and molecules

We describe here few selected applications for HHG spectroscopy of atoms and molecules by means of the RT-TDWF and the RT-TDDFT methods reviewed in Section 2. However, it worth mentioning that plenty of theoretical works based on physical models on one-active electron and/or few-dimensional descriptions of the spectroscopic target have been dedicated to HHG simulations [4, 5, 29, 33, 59–61, 68, 70, 187–194]. Other than atomic hydrogen [60, 61, 69, 70, 193, 194], HHG spectra of one-dimensional Be [135, 138] and C atoms [138],  $\text{H}_2^+$  [62, 68, 187, 190, 195],  $\text{D}_2^+$  [196, 197],  $\text{H}_3^{3+}$  and  $\text{H}_4^{3+}$  [192],  $\text{H}_2$  (also the full-electron three-dimensional molecule) [96, 111, 126, 190, 198–201],  $\text{T}_2$ ,  $\text{HeH}^+$  and  $\text{HeT}^+$  [202],  $\text{BC}^{2+}$  [135] have been computed. Coupling between electronic and nuclear degrees of freedom and its effect on HHG spectra has been also investigated [196, 197, 202].

HHG spectra from many-electron atoms and cations may encode interesting features, as giant enhancement [128], Cooper minimum [114, 124, 140], spin-orbit dependence of HHG spectrum [127], and electron correlation [59]. An accurate electron-structure description is necessary for capturing all these effects [115, 124, 127, 128, 130, 136, 140, 203, 204], i.e. going beyond single-active electron approximation. In Figure 1 we report the results for giant enhancement in Xe due to different recombination channels [128]. First, the electron is extracted from the  $5p_0$  orbital of Xe atom (step (1) in left panel of Figure 1A). After propagation, the electron collides with the parent ion, according to the 3SM (step (2)). Recombination steps follow two competitive channels: the electron fills the  $5p_0$  hole (step (3.1)), or the electron recombines with a more bound  $4d$  orbital, following the promotion of a second electron from the  $4d$  shell to the  $5p_0$  hole via Coulomb interaction (step (3.2)). HHG spectra from grid-based TD-CIS calculations using a pulse with intensity  $I = 1.7 \times 10^{14}$  W/cm<sup>2</sup>, a wavelength of 1500 nm and FWHM=10 fs, are reported in Figure 1B. The spectrum labelled by “inter+intra: all m” corresponds to a full TD-CIS calculation including all the nine  $4d$ ,  $5s$ , and  $5p$  atomic orbitals, and the “inter+intra: m=0” spectrum includes only the orbitals aligned with the pulse; in both cases interchannel (i.e., two-electron Coulomb interaction) and intrachannel couplings are active. The “intra: all m” spectrum accounts for the all nine orbitals with only intrachannel couplings included. One observes the giant enhancement only when interchannel interaction is included in the model, with an intensity increase in the 60-125 eV region for the “inter+intra: all m” case, and in the 60-90 eV energy window for the “inter+intra: m=0” simulation. Only a plateau in the HHG spectrum is instead found when interchannel couplings are excluded, thus showing that a multiple-orbital and multi-electron effect is responsible for the giant enhancement of HHG signal in xenon.

Single harmonics lying close to strong absorption/emission lines from transition metals can be strongly enhanced [205]. Experimental evidence suggests that an enhancement of the HHG pattern of Mn and  $\text{Mn}^+$  is originated by a  $3p$ - $3d$

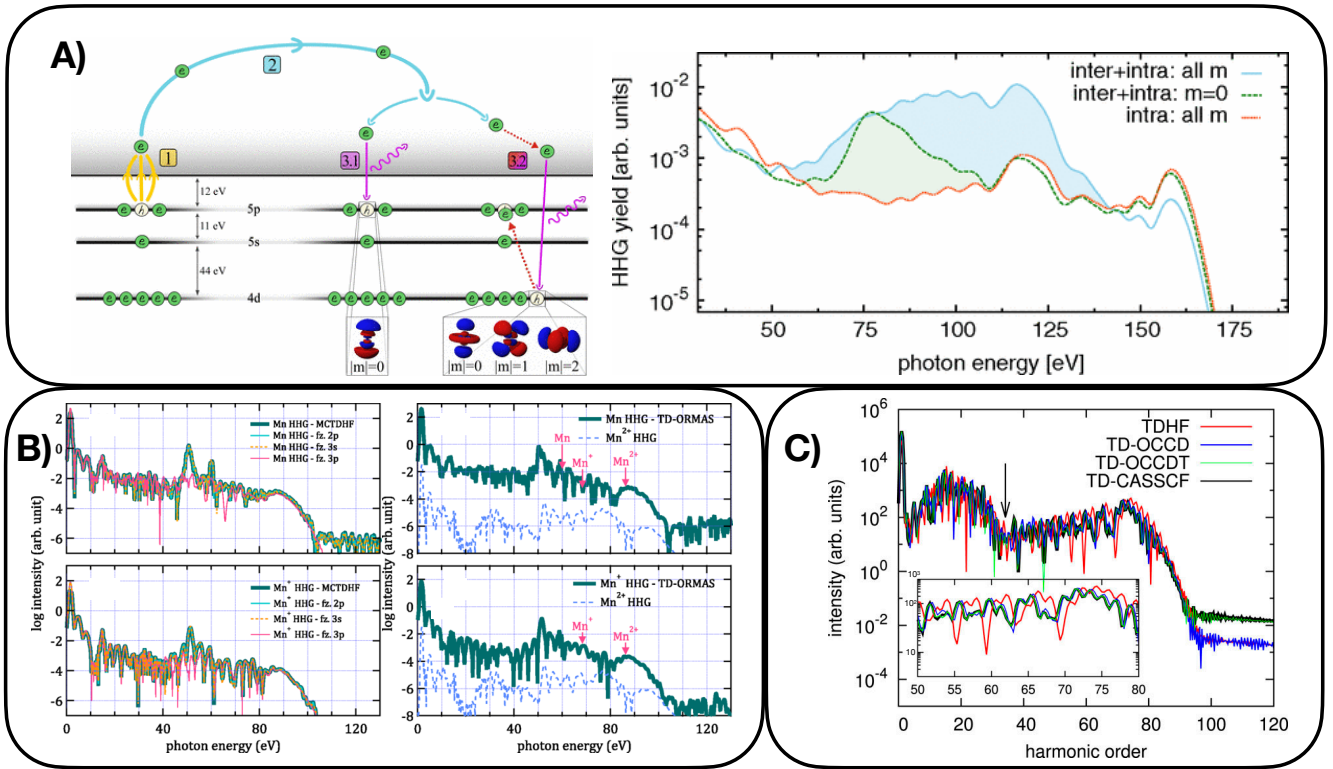


**Figure 1:** A). Left: Sketch representation of HHG dynamics in xenon. Right: HHG spectrum of xenon for different theoretical models (see text for details). B). Left: HHG spectra calculated with the TD-CASSCF method for several frozen-core settings for Mn and Mn<sup>+</sup>. Also MCTDHF spectrum is shown. Right: HHG spectra calculated with the TD-ORMAS method for Mn and Mn<sup>+</sup> (dark green). The vertical arrows indicate the 3SM the cutoff positions. The HHG spectrum from Mn<sup>2+</sup> obtained using TD-CASSCF with 14 orbitals is also plotted (dashed blue). C) Comparison of the HHG spectra of Ar atom by TDHF, TD-OCCD, TD-OCCDT, and TD-CASSCF methods. The inset the HHG spectra between H50 and H80, with HHG intensity in the  $10^{-3}$  range (in arbitrary units). Adapted from Ref. [114, 128, 136] with permission of American Physics Society and AIP Publishing.

resonance [205]. HHG spectra from Mn and Mn<sup>+</sup> at MCTDHF and TD-CASSCF level are reported in left panel of Figure 1B, and TD-ORMAS HHG spectra for Mn and Mn<sup>+</sup> and TD-CASSCF spectra for Mn<sup>2+</sup> are shown in right panel of Figure 1B. Spectra were obtained by using a pulse with a 770 nm central wavelength and an intensity of  $3 \times 10^{14}$  W/cm<sup>2</sup>. The high peak at around 50 eV is absent only when 3p orbitals are not included in the calculation (“fz.3p” label in left panel of Figure 1B). The enhancement is accurately described by MCTDHF and TD-CASSCF with various frozen-core approximations (“fz.2p” and “fz.3s”), meaning that 2p and 3s orbitals do not play role in harmonic enhancement, as suggested by the experiment [205]. TD-ORMAS calculation for Mn and Mn<sup>+</sup> provide the same conclusions. Intensity of Mn<sup>2+</sup> spectra is substantially lower than that from Mn and Mn<sup>+</sup> HHG because of the much larger ionisation energy.

The third example on atomic HHG spectra is reported in Figure 1C, where argon spectra computed using TDHF, TD-CASSCF, TD-OCCD and TD-OCCDT are reported [114]. Intensity and pulse wavelength are equal to  $6 \times 10^{14}$  W/cm<sup>2</sup> and 800 nm, respectively. A real-space grid basis set was employed to represent the electronic wavefunction, as for the results for Mn, Mn<sup>+</sup> and Mn<sup>2+</sup>. For TD-CASSCF, TD-OCCD and TD-OCCDT the neon core was kept frozen at HF molecular orbitals. In this case the HHG spectra are computed as Fourier transform of the time-dependent acceleration [70, 114]. Cooper minimum is correctly predicted by all the methods at around H34 (53 eV), in agreement with the experimental estimation of 48-54 eV [206–208]. The inset for H50-H80 shows that TD-CASSCF, TD-OCCD and TD-OCCDT are nearly identical at high energy. Instead, TDHF fails to reproduce fine structure of the HHG spectrum, which presents an high noise and even peaks.

RT-TDDFT calculations on HHG for He, Ne and Ar were also carried out to study the effect of SIC on the atomic nonlinear response [209].

A number of time-dependent ab initio electronic-structure approaches to many-electron molecular HHG is present in literature: N<sub>2</sub> [111, 210–214], CO [203, 211], BF and HF [211], F<sub>2</sub> [210, 211, 214], CO<sub>2</sub> [73, 215–217], OCS [216–218], CS<sub>2</sub> [218], C<sub>2</sub>H<sub>2</sub> [219], N<sub>2</sub>O [126, 217, 220], Br<sub>2</sub> [221], 1,2-dichloroethene [168], benzene [212, 222, 223], uracil and

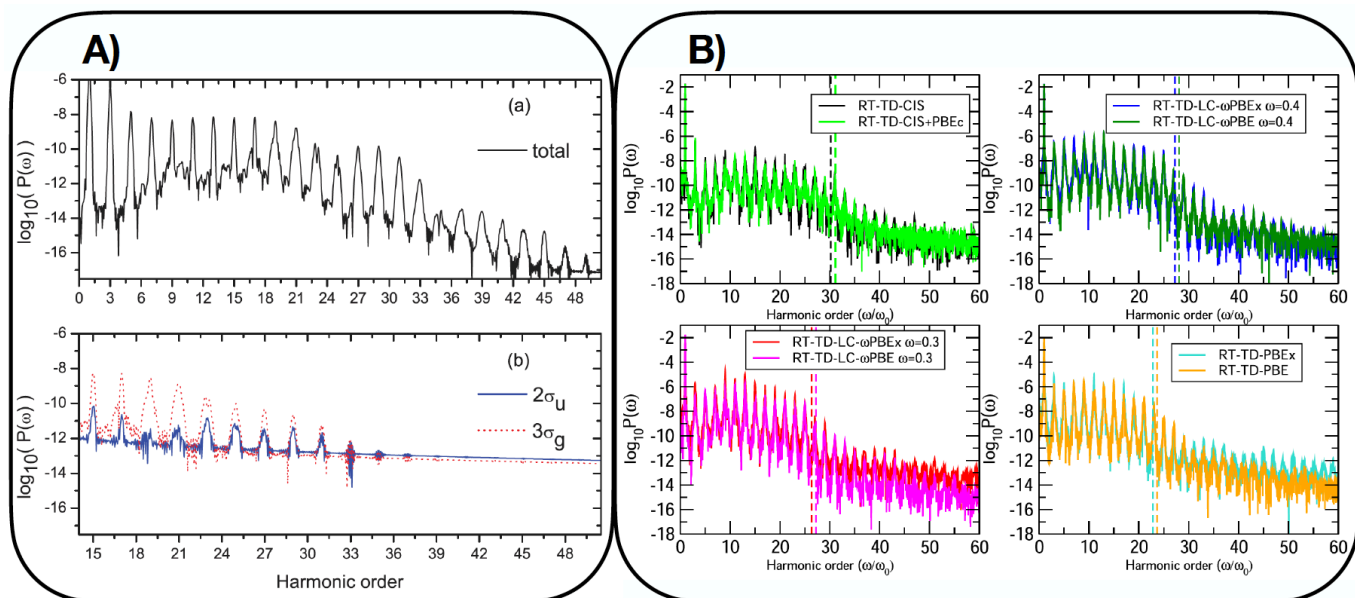


**Figure 2:** A): RT-TDDFT total spectrum of N<sub>2</sub> (upper panel) and orbital contributions to the HHG signal (lower panel). B): HHG spectrum of N<sub>2</sub> with various flavours of theory for the electronic wavefunction. TD-CIS+PBEc means that PBE correlation has been added to CIS description. The subscript x indicates that only exchange contribution is considered in the TDDFT calculations. In both cases the pulse is linearly polarised along the molecular axis, with an intensity of  $10 \times 10^{14}$  W/cm<sup>2</sup>, wavelength of 800 nm and duration of 20 optical cycles. Adapted from Refs [111, 211] with permission of American Physics Society and AIP Publishing.

thymine nucleobases [125].

The first two applications presented here are about N<sub>2</sub> and CO<sub>2</sub> in Figures 2 and 3 respectively, which have been widely studied experimentally for resolving the contribution of different molecular orbitals to the HHG signal [207, 224–226]. The (relatively) limited size of the two molecules made them particularly suitable for testing different levels of theory on strong-field electron dynamics.

RT-TDDFT was extensively used to study the HHG spectrum of N<sub>2</sub> by means of two different approaches: real-time propagation of time-dependent KS orbitals (Section 2.3), and real-time propagation of the electronic expressed in terms of singly-excited pseudo wavefunctions [111, 147] (Section 2.3). Spectra in Figure 2 were computed using a pulse linearly polarised along the molecular axis, with an intensity of  $10^{14}$  W/cm<sup>2</sup>, wavelength of 800 nm and time duration of 20 optical cycles. In the upper panel of Figure 2A the HHG total spectrum of N<sub>2</sub> is reported, whereas the  $3\sigma_g$  (HOMO) and  $2\sigma_u$  (HOMO-2) orbital contributions to the HHG signal are given in lower panel of Figure 2A. The LB $\alpha$  potential was employed [211]. The  $3\sigma_g$  contribution is dominant up to H31. At higher harmonics,  $2\sigma_u$  and  $3\sigma_g$  HHG intensities are comparable, even though peaks are only slightly higher than the background. Results from propagating TDSE using CIS and TDDFT eigenstates are reported in Figure 2B. In Ref. [111] the role of exchange and correlation in HHG was explored. Pulse parameters are the same reported above for Figure 2A. CIS, PBE and LC- $\omega$ PBE eigenstates were used. In the case of the long-range corrected LC- $\omega$ -PBE the separation parameter  $\omega$  has the value of 0.3 and 0.4. Comparison among the different approximations for the exchange term, i.e. CIS vs DFT using LC- $\omega$ -PBE, and for the correlation one (the PBE correlation was added/removed in the electronic computation) shows that HHG spectra are not dramatically affected by the choice of the level of theory. All the methods produce very similar HHG spectra, which are not very sensitive to the chosen description of exchange and correlation and/or to the correct asymptotic behaviour of the Coulomb potential. A further investigation using e.g. range-separated functions would be desirable to go deeper into the effect of long-range xc terms on the HHG spectrum.

As an example of strong-field molecular TDSE based on ADC electronic structure, we report here a recent study [73] on HHG dynamics in CO<sub>2</sub> (Figure 3). Electronic states were represented by a B-splines basis set. In the upper panel of Figure 3 results on the position of the intensity minimum as a function of pulse amplitude are reported. ADC(1) calculations reproduce the experimental dynamical behaviour of the minimum in the HHG spectrum: H19 for  $I = 0.6 \times 10^{14}$  W/cm<sup>2</sup>, H23 for  $I = 0.85 \times 10^{14}$  W/cm<sup>2</sup> and H27 for  $I = 1.1 \times 10^{14}$  W/cm<sup>2</sup>. The time duration is of 70 fs, the central wavelength is equal to 800 nm, and the pulse is linearly polarised along the molecular axis. These results originates from a dynamical interaction among different ionisation and recombination channels, as schematically reported in the lower panel of Figure 3. Steps 1.1, 2.1 and 3.1 follow the 3SM. The electron is mainly removed from the  $\pi_g$  and  $\sigma_u$

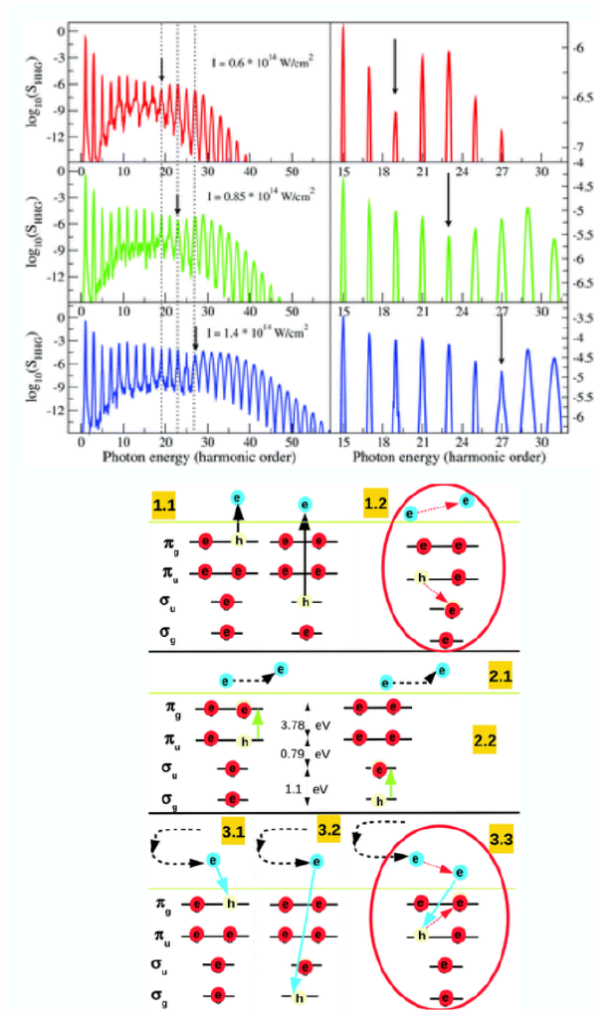


**Figure 3:** Upper panel: ADC(1) HHG spectrum of the  $\text{CO}_2$  molecule interacting with an infrared field. The laser field is linearly polarised along the molecular axis. Lower panel: Schematic illustration of the HHG process in  $\text{CO}_2$  using ADC(1). Taken from Ref. [73] with permission of the Royal Society of Chemistry.

orbitals by the intense pulse (1.1), provided the simulation parameters reported above. Correlation assisted tunneling (1.2) can occur, with the  $\pi_u$  channel interacting with the  $\sigma_u$  one. In the second step, the electron is accelerated in the continuum and then accelerates back towards the parent ion (2.1); empty  $1^2\Pi_u$  and  $1^2\Sigma_g^+$  excited ionic states can be populated by laser-induced dipole transitions between the  $\pi_g$ ,  $\sigma_u$  and the  $\pi_u$ ,  $\sigma_g$  orbitals respectively (2.2). Electron recombines with the ion in third step, following three possible pathways: the colliding electron fills back the same hole in step 1 (3.1) or the hole created in step 2.2 (3.2), or alternatively the electron exchanges energy with the ion by promoting ionic transitions between occupied and empty molecular orbitals (3.3). Correlation-driven effects, as those described above, can only be described thanks to an ab initio description of the propagating electronic wavefunction.

Recording HHG spectra of uracil and thymine molecules required laser ablation due to the difficulty of vaporising the samples [227]. HHG spectra are therefore the result of several effects: single-emitter signal from a number of fragments, different intensity of such a signal as a consequence of the mass/charge ratio, and phase matching/mismatching. For all these reasons, simulating the outcome of this experiment is extremely challenging. From a quantum-chemistry point of view, including a large number of electronic states (of the order of  $10^2$ - $10^3$ ) in strong-field TDSE is not a trivial task. The starting point in Ref. [125] was the simulation of single uracil and thymine molecules, by means of TD-CIS with the 3aug-cc-pVDZ+3K Gaussian basis set: 501 electronic states were considered for electron dynamics. K functions are GTOs optimal for the continuum [163], as mentioned in Section 2.4. Since the experimental setup did not include molecular alignment, simulated rotationally-averaged spectra of the single emitter were computed. HHG spectra from randomly-oriented molecules were computed in Ref. [125] by averaging over a number of random polarisation directions of the pulse. This allows us to remove even harmonics in the limit of a spherical distribution

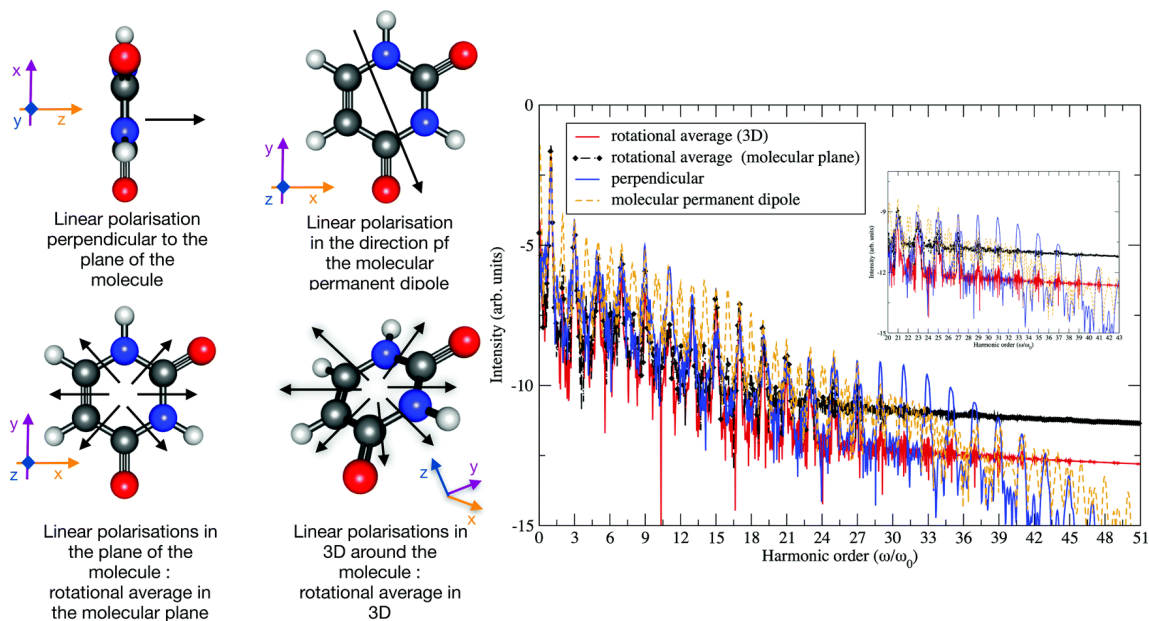


**Figure 4:** HHG spectra of uracil with pulse wavelength and intensity of 780 nm and  $10^{14}$  W/cm<sup>2</sup>, using a three-dimensional and molecule-plane average, a pulse linearly polarised perpendicular to the molecular plane and along the ground-state dipole moment. A zoom between H20 and H43 is also given. Adapted from Ref. [125] with permission of the Royal Society of Chemistry.

of polarisation directions. A polarisation vector  $\hat{\mathbf{n}}_s = (\hat{n}_{s,x}, \hat{n}_{s,y}, 0)$  was used for an average in the molecular plane (assumed to be the  $xy$  plane), whereas the vector  $\hat{\mathbf{n}}_s = (\hat{n}_{s,x}, \hat{n}_{s,y}, \hat{n}_{s,z})$  was selected for a full three-dimensional (3D) case. The components  $\hat{n}_{s,x}$  and  $\hat{n}_{s,y}$  (and also  $\hat{n}_{s,z}$  for the 3D case) are uniform random numbers in  $[-1:1]$  range fulfilling the conditions  $(\hat{n}_{s,x}^2 + \hat{n}_{s,y}^2 + \hat{n}_{s,z}^2) < 1$  or  $(\hat{n}_{s,x}^2 + \hat{n}_{s,y}^2) < 1$ . The averaged time-dependent dipole  $\bar{\boldsymbol{\mu}}(t)$  is given by

$$\bar{\boldsymbol{\mu}}(t) = \frac{1}{S} \sum_s \boldsymbol{\mu}_s(t) \cdot \hat{\mathbf{n}}_s, \quad (18)$$

where  $S$  is the number of different pulse linear polarisations  $\hat{\mathbf{n}}_s$  and  $\boldsymbol{\mu}_s(t)$  is the corresponding time-dependent dipole. The averaged HHG spectrum is then calculated as Fourier transform of the time-resolved dipole

$$\bar{P}_\mu(\omega) = \left| \frac{1}{t_f - t_i} \int_{t_i}^{t_f} W(t) \bar{\boldsymbol{\mu}}(t) e^{-i\omega t} dt \right|^2, \quad (19)$$

analogously to Eq. 3 for the time-dependent nonaveraged  $\langle \Psi(t) | \hat{\xi} | \Psi(t) \rangle$ . The application of an ab initio full-electron approach to the strong-field dynamics of uracil reported in Ref. [125] goes in the direction to compute HHG spectra of molecules of biological interest [228, 229]. Figure 4 collects the HHG spectrum of uracil computed with pulse wavelength and intensity of 780 nm and  $10^{14}$  W/cm<sup>2</sup>: after a 3D average, a planar average, a single polarisation perpendicular to the molecular axis, and along the direction of the ground-state dipole. The two rotationally-averaged HHG spectra are very similar for the low-energy and plateau regions and show different shapes around the cutoff. Harmonics up to around H39-H41 are observed for the 3D average, whereas the molecular-plane average produces harmonics up to H27-H29. This result suggests that contributions to HHG from out-of-plane polarisations play a role for higher harmonics. Moreover, the HHG spectrum with polarisation perpendicular to the molecular plane strongly differs from the averaged spectra. From H9 to H11, the harmonics are much higher than those in the two averaged HHG spectra. The difference between averaged and perpendicular-polarisation spectra can be rationalised by examining the possible ionisation channels and their symmetry, as explained in Ref. [125].

HHG spectroscopy has been proposed as a method to discriminate molecular isomers [77, 230]. This approach represents an original way to study the coupling between geometric features and ultrafast electron dynamics in strong fields. Experimentally, authors of Ref. [77] observed that the cis form of 1,2-dichloroethene (DCE) and 2-butene has a more

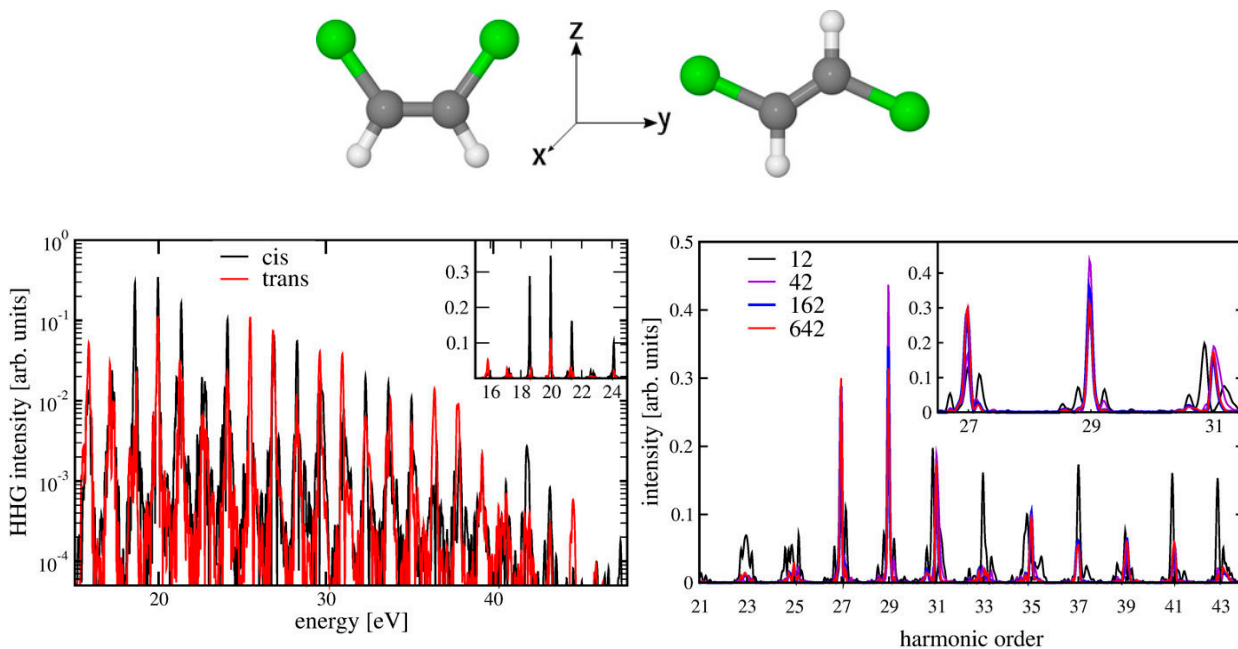


**Figure 5:** HHG spectra of cis and trans DCE. Left: rotationally averaged HHG spectra of cis-DCE (black) and trans-DCE (red). The inset shows the linear intensity of HHG signals in an energy range between 16 eV and 24 eV, corresponding to harmonics 23-35. Right: Rotationally averaged HHG spectra of cis-DCE computed with TD-CIS and a different number of laser polarisations (12, 42, 162, 642). The intensity is plotted on a linear scale as a function of the H21-H43. Adapted from Ref. [168] with permission of AIP Publishing.

intense HHG signal than the trans isomer by 8 and 5 times respectively. A time-resolved HHG approach has been developed in Ref. [230], in which the HHG signal was probed along the fast photoisomerisation of 1,3-cyclohexadiene, leading to ring opening with the formation of 1,3,5-hexatriene. TD-CIS calculations on cis and trans forms of DCE were recently performed, using the aug-cc-pVTZ Gaussian basis set enriched by diffuse GTOs due to a ghost atom placed at the center of charge of the molecule. Ionisation was taken into account by using both the heuristic lifetime model and a real-space CAP. To simulate random alignment, the total HHG spectrum was obtained by averaging the time-dependent dipole over 162 pulse polarisations (left panel of Figure 5). The polarisation vectors are uniformly distributed on the surface of a sphere by means of the subdivision of an icosahedron [168]. A pulse intensity of  $1.1 \times 10^{14}$  W/cm<sup>2</sup> and a wavelength of 1800 nm were used, according to the original experiment [77]. Low- and medium-energy harmonics were reasonably described at theoretical level. Indeed, the comparison between the computed spectra in the energy window 16-24 eV (H23-H35) show the cis signal usually more intense than the trans signal, as reported in the experiment.

Convergence of the rotationally averaged HHG spectrum as a function of the number of pulse polarisations is reported for the cis DCE in right panel of Figure 5. H21-H43 interval is plotted. HHG spectra with 162 and 642 polarisations are substantially superimposed, clearly indicating that 162 simulations were enough to get a converged spectrum. Even harmonics are eliminated by increasing the number of polarisations, as already pointed out for uracil calculations in Figure 4.

Role of linear polarisation of the pulse in HHG of benzene molecule was investigated by means of real-space RT-TDDFT within the LDA in the exchange-only limit [212]. HHG spectra for perpendicular and parallel polarisation with respect to the molecular plane are presented in the upper panel of Figure 6. Pulse is characterised by a wavelength equal to 780 nm and peak intensity of  $4 \times 10^{14}$  W/cm<sup>2</sup>. Pulse duration is 10 optical cycles. A reduction of harmonic intensity in the cutoff region is observed in the case of pulse aligned parallel to the molecular plane. This result is explained in terms of “unfavored”  $\pi$  symmetry of HOMO [212], similarly to what was suggested for HHG in uracil and thymine [125].

A nonadiabatic molecular dynamics scheme [212, 222] was also developed to study the possibly coupled electronic and nuclear response to intense fields. The analysis was done focusing on the time evolution of KS orbitals, using the LADSIC exchange-correlation functional, as reported in lower panels of Figure 6. In this case a wavelength of 800 nm and a peak intensity of  $3.5 \times 10^{14}$  W/cm<sup>2</sup> were chosen for the simulations. In left (right) lower panel the time evolution

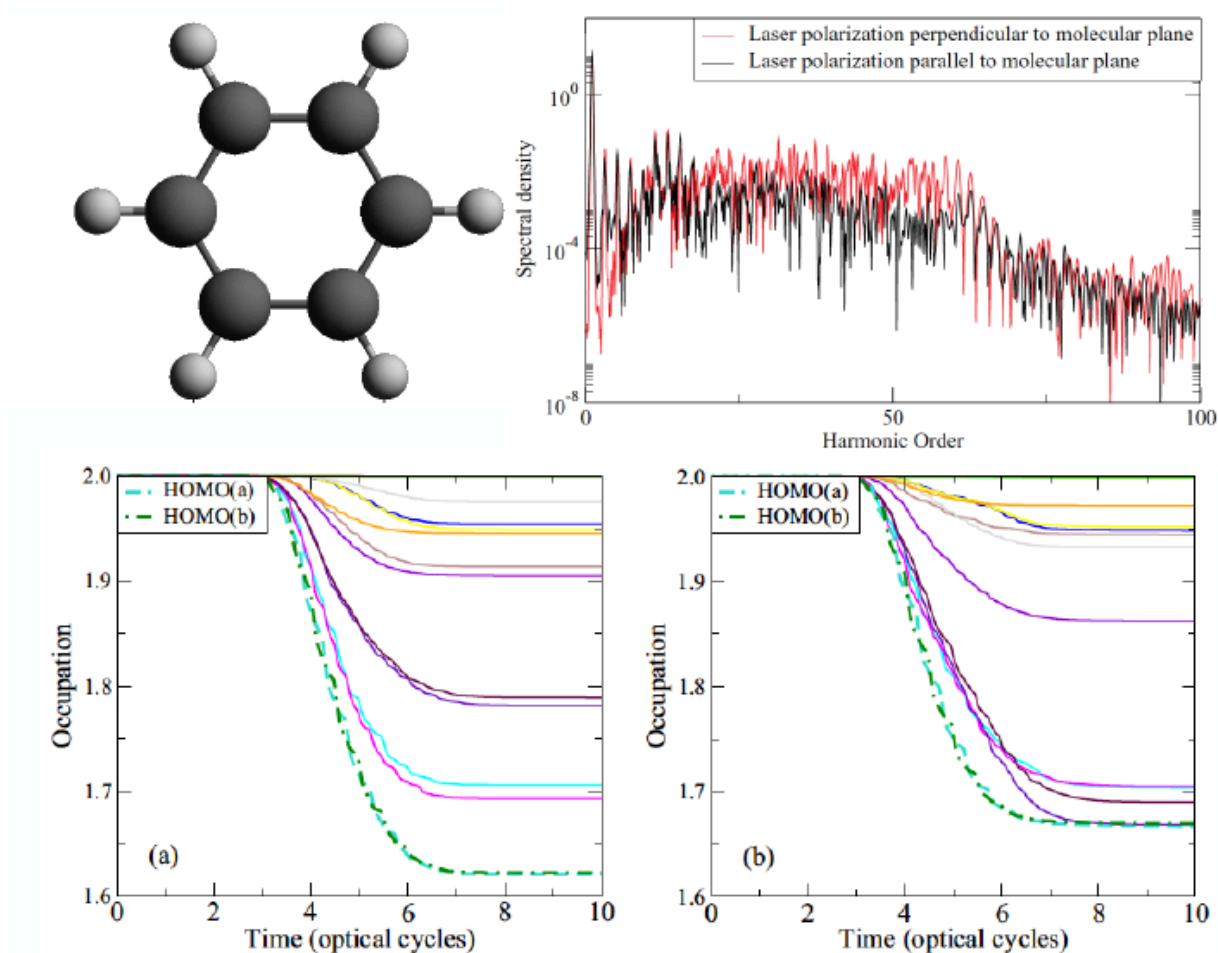


**Figure 6:** Upper panel: benzene HHG spectra for perpendicular (red) and parallel (blue) pulse polarisation with respect to the molecular plane. Lower panels [222]: Time evolution of populations of the KS. Frozen and moving nuclei in panel (a) and (b), respectively, with a pulse parallel polarisation. Only the two degenerate HOMO (HOMO(a) and HOMO(b)) are reported for sake of clarity. T Adapted from Ref. [212, 222] with permission of AIP Publishing and American Physics Society.

of KS orbitals with moving (frozen) ions are reported for a parallel pulse polarisation. Only the HOMO (with (a) (b) indicating two degenerate MOs) populations are labeled for sake of clarity. Decreasing of MO occupation is related to an increase of ionisation from that MO. One observes that the total HOMO occupation becomes smaller when nuclei are moved, which corresponds to a larger ionisation. However, for both frozen and moving nuclei, contributions from more bound MOs are not negligible, indicating a contributions to HHG from multiple MOs.

All the results collected in this Section refer to single-emitter spectra. Macroscopic contribution due to the propagation of the harmonic field in the sample can affect the shape and harmonic intensity of the HHG spectrum [231, 232]. Several attempts to combine the macroscopic response to an ab initio description of the molecular target have been proposed in literature, e.g. for Ar [233, 234],  $N_2$  [233] and  $N_2^+$  [235] moieties [235].

### 3.2. Solids

Simulating HHG from solids needs two major ingredients [41, 142]: an accurate description of microscopic effects via quantum methods for, and the inclusion of macroscopic features typically via the propagation of Maxwell equations. Focusing on the microscopic origin of HHG in solids, one can exclusively rely on ab initio approaches able to describe strong-field dynamics, as already outlined in Section 2, e.g. TDDFT [41, 46, 47, 142]. TDDFT has been applied to study the effect of the electronic structure on HHG from a prototype system such as bulk silicon [47]. In that work the pulse intensity was taken to be  $I=10^{11}$  W/cm<sup>2</sup>, and the pulse wavelength equal to 3000 nm. LDA was employed to propagate KS equations. In Figure 7A HHG spectra from full LDA propagation of KS equations and from frozen

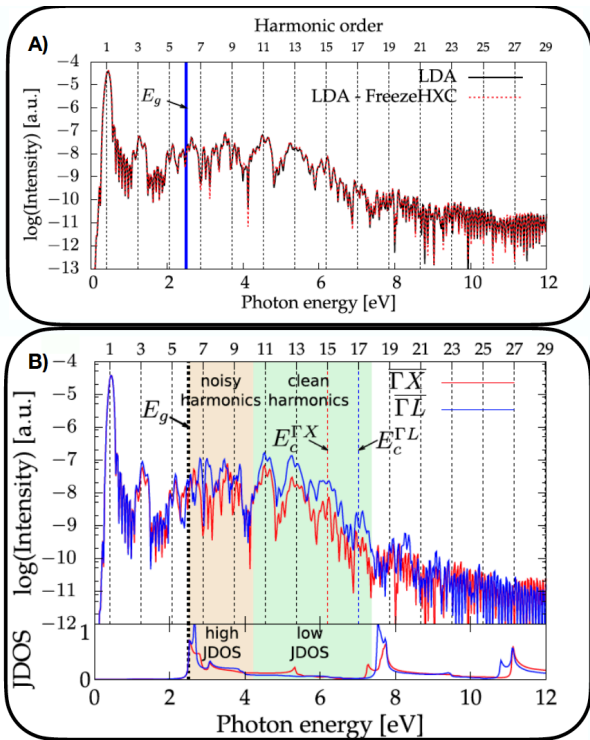


**Figure 7:** HHG spectra of bulk silicon. Panel A): Comparison of HHG spectra using a pulse polarization along  $\Gamma\bar{X}$ , computed by means of LDA and within LDA freezing the Coulomb and exchange-correlation terms to their ground-state value (LDA-FreezeHXC). Panel B): HHG spectra for the  $\Gamma\bar{X}$  (red line in the online version) and the  $\Gamma\bar{L}$  polarisation direction (blue line in the online version). JDOS is also given. Adapted from Ref. [47] with permission of American Physics Society.

(at the ground-state values) Coulomb and exchange-correlation terms are reported. The fact that the two spectra are nearly identical suggests that, in the used theory approximation and pulse conditions for the bulk silicon, electrons practically evolve as independent particles. Role of pulse polarisation is investigated in Figure 7B. Simulations on the cubic material were carried out by rotating the polarisation vector around the [001] crystallographic axis. HHG is maximum for a pulse polarisation along  $\Gamma\bar{K}$  and minimal for the  $\Gamma\bar{X}$  directions, respectively. One observes that HHG is anisotropic, with the  $\Gamma\bar{X}$  cutoff being larger (H17). Harmonics with energy below the band gap can not be originated by an electron-hole recombination due to an interband transition. On the other hand, harmonics above the band gap can be due to interband electron-hole recombination. In this situation, also intraband dynamics can contribute to harmonic emission. By inspecting HHG spectra and the joint density of states (JDOS), one can argue from Figure 7B that clean odd harmonics are found, for both polarisations, when the JDOS is small, i.e. when the contribution of interband transitions is negligible.

In Ref. [46] authors used time propagation of KS equations (using LDA) to study the evolution of the HHG response of hexagonal boron nitride (Figure 8A) from the monolayer to the bulk. Anisotropy of HHG response was investigated in terms of in-plane and out-of-plane contributions to the emitted signal. Pulse polarisation was linear along the  $\Gamma\bar{K}$  crystallographic direction, with wavelength of 1600 nm and FWHM equal to 15 (out-of-plane case) and 30 fs (in-plane case). The effect of layer stacking on in-plane HHG spectra is shown in the panel B of Figure 8. The applied pulse intensity is of  $7.02 \times 10^{13}$  W/cm<sup>2</sup>. Features of HHG spectra from the slabs rapidly converge to those of the bulk spectrum, as observed in upper figure. Since the small differences observed are due to surface effects, a more proper comparison is given in the bottom figure, where the HHG spectrum from the innermost layers of a 6-layer slab of boron nitride is nearly identical to the bulk one. Whereas the in-plane HHG response is not strongly modified by the number of layers, the layer stacking instead strongly affects the out-of-plane HHG spectra of boron nitride, as reported in Figure 8C. Intensity of low-energy harmonics increases with the number of layers, approaching the bulk result, as shown in the upper Figure 8C. For high-energy harmonics, however, the harmonic yield, integrated between 43 and 60 eV, is maximum for the bilayer system and decreases with the number of layers. This outcome is rationalised in terms of combined effect due to the induced electric field, the delocalisation of the wave functions among the layers, and the increasing number of ionised electrons.

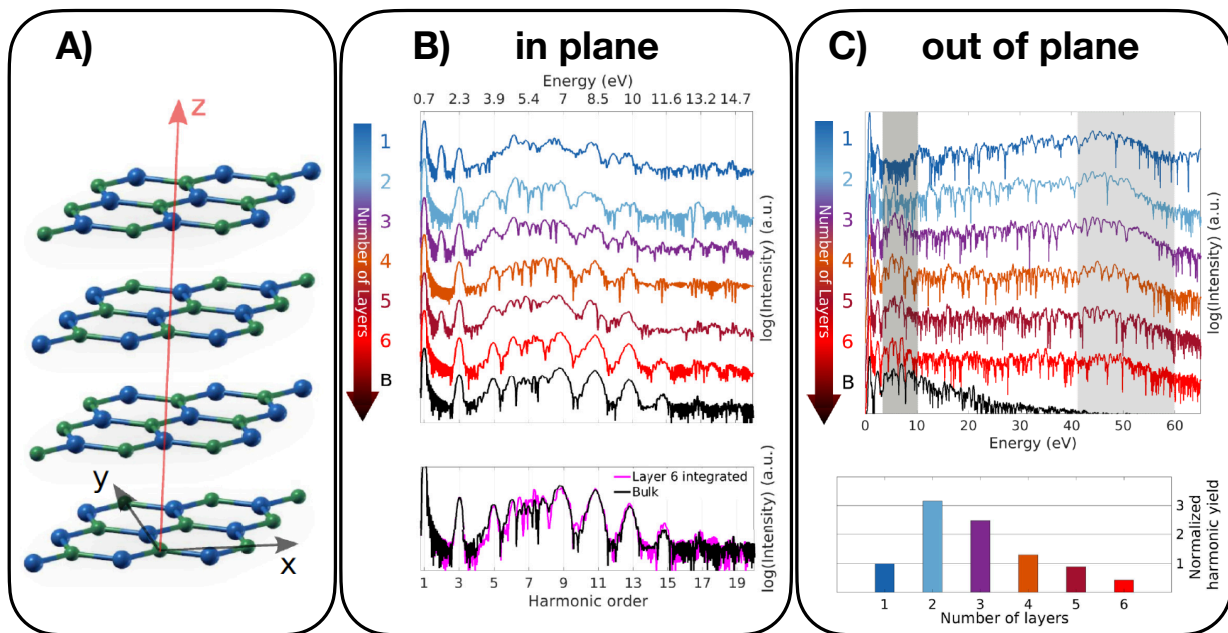


**Figure 8:** A): boron oxide layers (boron: blue, nitrogen: green). B) upper panel: in-plane HHG spectra of one- to six-layer slabs and for the bulk; bottom panel: comparison between the bulk HHG spectrum (black in online color version) and the spectrum obtained from the innermost layers of a six-layer slab. C) upper panel: out-of-plane HHG spectra of one- to six-layer slabs and for the bulk; bottom panel: integrated harmonic yield between 43 and 60 eV. Adapted from Ref. [46] with permission of American Physics Society.

#### 4. Conclusions and Outlook

In this Review we have collected the time-dependent *ab initio* techniques developed for strong-field dynamics and calculation of HHG spectra. Wave-function and density approaches, originally formulated for the prediction of bound-state properties, have been adapted to the real-time propagation of an electronic wavefunction under the influence of a very intense pulse, leading to RT-TDWF and RT-TDDFT methods. This theoretical/computational effort was needed to go beyond simplified models, and to properly describe the many-electron interaction characterising HHG in several systems.

We also report here some ideas for future developments of time-dependent *ab initio* methods applied to strong-field dynamics. As already pointed out in Section 2.4, the most challenging task is to combine computational efficiency of GTOs and accuracy in representing the continuum. Even though hybrid bases involving GTOs have already been formulated [170–172], their applicability was limited to small and/or model systems. Extension to larger molecular systems, such as benzene and nucleobases shown in Section 3, still represents a demanding task for theoreticians.

In electronic-structure calculations, a “third way” other than methods based on wave functions and density is provided by quantum Monte Carlo (QMC) approaches [236–241]. Formulation of QMC methods, which are a gold-standard for correlated time-dependent wavefunctions, in time domain could provide a valuable tool to unravel many-electron effects in strong-field dynamics of metal-based systems and solids. Same comment is extendable to Bethe-Salpeter equation (BSE), allowing one to go beyond TDDFT; BSE-based TDSE has been recently applied to study electron dynamics in linear regime [148], and could be formulated for strong-field processes.

HHG experiments on chiral molecules allow one to discriminate enantiomers by means of nonlinear response and to follow the time evolution of a chemical reaction with chiral intermediate species [33–37]. Adding magnetic and quadrupolar interaction in the TDSE is a needed step to account for the time-response of chiral moieties to circularly polarised electromagnetic fields with *ab initio* accuracy.

#### Acknowledgements

EC acknowledges funding from University of Trieste under the grants FRA and Microgrants 2020.

## References

- [1] Burnett N H, Baldis H A, Richardson M C and Enright G D 1977 *Applied Physics Letters* **31** 172–174 (Preprint <https://doi.org/10.1063/1.89628>) URL <https://doi.org/10.1063/1.89628>
- [2] McPherson A, Gibson G, Jara H, Johann U, Luk T S, McIntyre I A, Boyer K and Rhodes C K 1987 *J. Opt. Soc. Am. B* **4** 595–601 URL <http://www.osapublishing.org/josab/abstract.cfm?URI=josab-4-4-595>
- [3] Ferray M, L’Huillier A, Li X F, Lompre L A, Mainfray G and Manus C 1988 *Journal of Physics B: Atomic, Molecular and Optical Physics* **21** L31–L35 URL <https://doi.org/10.1088/0953-4075/21/3/001>
- [4] Lewenstein M, Balcou P, Ivanov M Y, L’Huillier A and Corkum P B 1994 *Phys. Rev. A* **49** 2117
- [5] Corkum P B 1993 *Phys. Rev. Lett.* **71** 1994
- [6] Paul P M, Toma E S, Breger P, Mullot G, Augé F, Balcou P, Muller H G and Agostini P 2001 *Science* **292** 1689
- [7] Sansone G 2020 *Nat. Photonics* **14** 131–133 ISSN 1749-4893
- [8] Gaumnitz T, Jain A, Pertot Y, Huppert M, Jordan I, Ardana-Lamas F and Wörner H J 2017 *Opt. Express* **25** 27506–27518
- [9] Chappuis C, Bresteau D, Auguste T, Gobert O and Ruchon T 2019 *Phys. Rev. A* **99**(3) 033806
- [10] Calegari F, Sansone G, Stagira S, Vozzi C and Nisoli M 2016 *J. Phys. B* **49** 062001
- [11] Nisoli M, Decleva P, Calegari F, Palacios A and Martín F 2017 *Chem. Rev.* **117** 10760
- [12] Geneaux R, Marroux H J B, Guggenmos A, Neumark D M and Leone S R 2019 *Phil. Trans. R. Soc. A* **377** 20170463
- [13] Kraus P M, Zürich M, Cushing S K, Neumark D M and Leone S R 2018 *Nat. Rev. Chem.* **2** 82
- [14] Dubrouil A, Hort O, Catoire F, Descamps D, Petit S, Mével E, Strelkov V V and Constant E 2014 *Nat. Commun.* **5** 4637
- [15] Mak A, Shamuilov G, Salén P, Dunning D, Hebling J, Kida Y, Kinjo R, McNeil B W J, Tanaka T, Thompson N, Tibai Z, Tóth G and Goryashko V 2019 *Reports on Progress in Physics* **82** 025901 URL <https://doi.org/10.1088/1361-6633/aafa35>
- [16] Krausz F and Ivanov M 2009 *Rev. Mod. Phys.* **81**(1) 163–234 URL <https://link.aps.org/doi/10.1103/RevModPhys.81.163>
- [17] Leone S R and Neumark D M 2016 *Faraday Discuss.* **194**(0) 15–39 URL <http://dx.doi.org/10.1039/C6FD00174B>
- [18] Zewail A H 2000 *The Journal of Physical Chemistry A* **104** 5660–5694 (Preprint <https://doi.org/10.1021/jp001460h>) URL <https://doi.org/10.1021/jp001460h>
- [19] Palacios A and Martín F 2020 *WIREs Computational Molecular Science* **10** e1430 (Preprint <https://wires.onlinelibrary.wiley.com/doi/pdf/10.1002/wcms.1430>) URL <https://wires.onlinelibrary.wiley.com/doi/abs/10.1002/wcms.1430>
- [20] Faccialá D, Pabst S, Bruner B D, Ciriolo G, De Silvestri S, Devetta M, Negro M, Soifer H, Stagira S, Dudovich N and Vozzi C 2016 *Phys. Rev. Lett.* **117** 093902
- [21] Bruner B D, Masin Z, Negro M, Morales F, Brambila D, Devetta M, Faccialá D, Harvey A G, Ivanov M, Mairesse Y, Patchkovskii S, Serbinenko V, Soifer H, Stagira S, Vozzi C, Dudovich N and Smirnova O 2016 *Faraday Discuss.* **194** 369
- [22] Marciniak A, Despré V, Lorio V, Karra G, Heré M, Quinta L, Catoi F, Jobl C, Consta E and Lépine A I K F 2019 *Nat. Commun.* **10** 337
- [23] Ossiander M, Siegrist F, Shirvanyan V, Pazourek R, Sommer A, Latka T, Guggenmos A, Nagele S, Feist J, Burgdörfer J, Kienberger R and Schultze M 2017 *Nat. Phys.* **13** 280
- [24] Peng P, Marceau C and Villeneuve D M 2019 *Nat. Rev. Phys.* **1** 144–155
- [25] Vozzi C, Negro M, Calegari F, Sansone G, Nisoli M, Silvestri S D and Stagira S 2011 *Nat. Phys.* **7** 822
- [26] Negro M, Devetta M, Faccialá D, De Silvestri S, Vozzi C and Stagira S 2014 *Faraday Discuss.* **171** 133
- [27] Haessler S, Caillat J, Boutu W, Giovanetti-Teixeira C, Ruchon T, Auguste T, Diveki Z, Breger P, Maquet A, Carré B, Taïeb R and Salières P 2010 *Nature Phys.* **6** 200–206
- [28] Catoire F, Bachau H, Wang Z, Blaga C, Agostini P and DiMauro L F 2018 *Phys. Rev. Lett.* **121** 143902
- [29] Tuthill D R, Mauger F, Scarborough T D, Jones R R, Gaarde M B, Lopata K, Schafer K J and DiMauro L F 2020 *J. Mol. Spectrosc.* **372** 111354
- [30] Li W, Zhou X, Lock R, Patchkovskii S, Stolow A, Kapteyn H C and Murnane M M 2008 *Science* **322** 1207
- [31] Coccia E 2020 *Mol. Phys.* **118** e1769871
- [32] Marangos J 2016 *J. Phys. B* **49** 132001
- [33] Cireasa R, Boguslavskiy A E, Pons B, Wong M C H, Descamps D, Petit S, Ruf H, Thiré N, Ferré A, Suarez J, Higué J, Schmidt B E, Alharbi A F, Légaré F, Blanchet V, Fabre B, Patchkovskii S, Smirnova O, Mairesse Y and Bhardwaj V R 2015 *Nat. Phys.* **11** 654
- [34] Baykusheva D, Zindel D, Svoboda V, Bommeli E, Ochsner M, Tehlar A, and Wörner H J 2019 *Proc Natl Acad Sci USA* **116** 23923
- [35] Harada Y, Haraguchi E, Kaneshima K and Sekikawa T 2018 *Phys. Rev. A* **98** 021401
- [36] Ayuso D, Neufeld O, Ordonez A F, Decleva P, Lerner G, Cohen O, Ivanov M and Smirnova O 2019 *Nat. Photonics* **13** 866
- [37] Baykusheva D and Wörner H J 2018 *Phys. Rev. X* **9** 031060
- [38] Ghimire S, DiChiara A D, Sistrunk E, Agostini P, DiMauro L F and Reis D A 2011 *Nature Physics* **7** 138–141 ISSN 1745-2481 URL <https://doi.org/10.1038/nphys1847>
- [39] Ghimire S and Reis D A 2019 *Nature Physics* **15** 10–16 ISSN 1745-2481 URL <https://doi.org/10.1038/s41567-018-0315-5>
- [40] Hansen K K, Bauer D and Madsen L B 2018 *Phys. Rev. A* **97**(4) 043424 URL <https://link.aps.org/doi/10.1103/PhysRevA.97.043424>
- [41] Yamada S and Yabana K 2021 *Phys. Rev. B* **103**(15) 155426 URL <https://link.aps.org/doi/10.1103/PhysRevB.103.155426>
- [42] Cox J D, Marini A and de Abajo F J G 2017 *Nature Communications* **8** 14380 ISSN 2041-1723 URL <https://doi.org/10.1038/ncomms14380>
- [43] Vampa G, Ghamsari B G, Siadat Mousavi S, Hammond T J, Olivieri A, Lisicka-Skrek E, Naumov A Y, Villeneuve D M, Staudte A, Berini P and Corkum P B 2017 *Nature Physics* **13** 659–662 ISSN 1745-2481 URL <https://doi.org/10.1038/nphys4087>
- [44] Han S, Kim H, Kim Y W, Kim Y J, Kim S, Park I Y and Kim S W 2016 *Nature Communications* **7** 13105 ISSN 2041-1723 URL <https://doi.org/10.1038/ncomms13105>
- [45] Sivilis M, Taucer M, Vampa G, Johnston K, Staudte A, Naumov A Y, Villeneuve D M, Ropers C and Corkum P B 2017 *Science* **357** 303–306
- [46] Le Breton G, Rubio A and Tancogne-Dejean N 2018 *Phys. Rev. B* **98**(16) 165308 URL <https://link.aps.org/doi/10.1103/PhysRevB.98.165308>
- [47] Tancogne-Dejean N, Mücke O D, Kärtner F X and Rubio A 2017 *Phys. Rev. Lett.* **118**(8) 087403 URL <https://link.aps.org/doi/10.1103/PhysRevLett.118.087403>
- [48] Catoire F, Bachau H, Wang Z, Blaga C, Agostini P and DiMauro L F 2018 *Phys. Rev. Lett.* **121**(14) 143902 URL <https://link.aps.org/doi/10.1103/PhysRevLett.121.143902>
- [49] Klemke N, Mücke O D, Rubio A, Kärtner F X and Tancogne-Dejean N 2020 *Phys. Rev. B* **102**(10) 104308 URL

- <https://link.aps.org/doi/10.1103/PhysRevB.102.104308>
- [50] Tancogne-Dejean N, Mücke O D, Kärtner F X and Rubio A 2017 *Nature Communications* **8** 745 ISSN 2041-1723 URL <https://doi.org/10.1038/s41467-017-00764-5>
- [51] Hohenleutner M, Langer F, Schubert O, Knorr M, Huttner U, Koch S W, Kira M and Huber R 2015 *Nature* **523** 572–575 ISSN 1476-4687 URL <https://doi.org/10.1038/nature14652>
- [52] Vampa G, Hammond T J, Thiré N, Schmidt B E, Légaré F, McDonald C R, Brabec T and Corkum P B 2015 *Nature* **522** 462–464 ISSN 1476-4687 URL <https://doi.org/10.1038/nature14517>
- [53] You Y S, Yin Y, Wu Y, Chew A, Ren X, Zhuang F, Gholam-Mirzaei S, Chini M, Chang Z and Ghimire S 2017 *Nature Communications* **8** 724 ISSN 2041-1723 URL <https://doi.org/10.1038/s41467-017-00989-4>
- [54] Li J, Lu J, Chew A, Han S, Li J, Wu Y, Wang H, Ghimire S and Chang Z 2020 *Nature Communications* **11** 2748 ISSN 2041-1723 URL <https://doi.org/10.1038/s41467-020-16480-6>
- [55] Santra R and Gordon A 2006 *Phys. Rev. Lett.* **97** 073906
- [56] Gordon A, Kärtner F, Rohringer N and Santra R 2006 *Phys. Rev. Lett.* **96** 223902
- [57] Smirnova O, Mairesse Y, Patchkovskii S, Dudovich N, Villeneuve D, Corkum P and Ivanov M Y 2009 *Nature* **460** 972
- [58] Beaulieu S, Camp S, Descamps D, Comby A, Wanie V, Petit S, Légaé F, Schafer J, Gaarde B, Catoire F, and Mairesse Y 2016 *Phys. Rev. Lett.* **117** 203001
- [59] Kraus P M and Wörner H J 2018 *Angew. Chem. Int. Ed.* **57** 5228
- [60] Krause J L, Schafer K J and Kulander K C 1992 *Phys. Rev. A* **45** 4998
- [61] Han Y C and Madsen L B 2010 *Phys. Rev. A* **81** 063430
- [62] Ruiz C, Plaja L, Taïeb R, Veniard V and Maquet A 2006 *Phys. Rev. A* **73** 063411
- [63] Gordon A, Kärtner F X, Rohringer N and Santra R 2006 *Phys. Rev. Lett.* **96**(22) 223902 URL <https://link.aps.org/doi/10.1103/PhysRevLett.96.223902>
- [64] Taïeb R, Vénierard V, Wassaf J and Maquet A 2003 *Phys. Rev. A* **68** 033403
- [65] Yu C, Jiang S and Lu R 2019 *Advances in Physics: X* **4** 1562982 (Preprint <https://doi.org/10.1080/23746149.2018.1562982>) URL <https://doi.org/10.1080/23746149.2018.1562982>
- [66] Bedurke F, Klamroth T and Saalfrank P 2021 *Phys. Chem. Chem. Phys.* **23** 13544
- [67] Luppi E and Head-Gordon M 2012 *Mol. Phys.* **110** 909
- [68] Labeye M, Zapata F, Coccia E, Veniard V, Toulouse J, Caillat J, Taïeb R and Luppi E 2018 *J. Chem. Theory Comput.* **14** 5846
- [69] Coccia E and Luppi E 2016 *Theor. Chem. Acc.* **135** 43
- [70] Coccia E, Mussarab B, Labeye M, Caillat J, Taïeb R, Toulouse J and Luppi E 2016 *Int. J. Quant. Chem.* **116** 1120
- [71] Coccia E, Assaraf R, Luppi E and Toulouse J 2017 *J. Chem. Phys.* **147** 014106
- [72] Caillat J, Zanghellini J, Kitzler M, Koch O, Kreuzer W and Scrinzi A 2005 *Phys. Rev. A* **71** 012712
- [73] Ruberti M, Decleva P and Averbukh V 2018 *Phys. Chem. Chem. Phys.* **20** 8311
- [74] Nest M, Padmanaban R and Saalfrank P 2007 *J. Chem. Phys.* **126** 214106
- [75] Sato T and Ishikawa K L 2015 *Phys. Rev. A* **91** 023417
- [76] Sato T, Ishikawa K L, Brezinová I, Lackner F, Nagele S and Burgdörfer J 2016 *Phys. Rev. A* **94** 023405
- [77] Wong M C H, Brichta J P, Spanner M, Patchkovskii S and Bhardwaj V R 2011 *Phys. Rev. A* **84** 051403(R)
- [78] Bedurke F, Klamroth T, Krause P and Saalfrank P 2019 *J. Chem. Phys.* **150** 234114
- [79] Tikhomirov I, Sato T and Ishikawa K L 2017 *Phys. Rev. Lett.* **118**(20) 203202
- [80] Krause P, Klamroth T and Saalfrank P 2005 *J. Chem. Phys.* **123** 074105
- [81] Huber C and Klamroth T 2005 *Appl. Phys. A* **87** 93
- [82] Krause P, Klamroth T and Saalfrank P 2007 *J. Chem. Phys.* **127** 034107
- [83] Rohringer N, Gordon A and Santra R 2006 *Phys. Rev. A* **74** 043420
- [84] Sato T and Ishikawa K L 2013 *Phys. Rev. A* **88** 023402
- [85] Greenman L, Ho P J, Pabst S, Kamarchik E, Mazziotti D A and Santra R 2010 *Phys. Rev. A* **82** 023406
- [86] S Bauch L K S and Madsen L B 2014 *Phys. Rev. A* **90** 062508
- [87] Tancogne-Dejean N, Oliveira M J T, Andrade X, Appel H, Borca C H, Le Breton G, Buchholz F, Castro A, Corni S, Correa A A, De Giovannini U, Delgado A, Eich F G, Flick J, Gil G, Gomez A, Helbig N, Hübenner H, Jestädt R, Jornet-Somoza J, Larsen A H, Lebedeva I V, Lüders M, Marques M A L, Ohlmann S T, Pipolo S, Rapp M, Rozzi C A, Strubbe D A, Sat S A, Schäfer C, Theophilou I, Welden A and Rubio A 2020 *J. Chem. Phys.* **152** 124119
- [88] Rossi T P, Kuisma M, Puska M J, Nieminen R M and Erhart P 2017 *J. Chem. Theory Comput.* **13** 4779
- [89] Wopperer P, Dinh P M, Reinhard P G and Suraud E 2015 *Phys. Rep.* **562** 1
- [90] Gao C Z, Dinh P M, Reinhard P G and Suraud E 2017 *Phys. Chem. Chem. Phys.* **19** 19784
- [91] Vincendon M, Lacombe L, Dinh P M, Suraud E and Reinhard P G 2017 *Comput. Mater. Sci.* **138** 426
- [92] Pilmè J, Luppi E, Berès J, Hoëe-Levin C and de la Lande A 2014 *J. Mol. Mod.* **20** 2368
- [93] Wu X, Teuler J M, Cailliez F, Clavaguera C, Salahub D R and de la Lande A 2017 *J. Chem. Theory Comput.* **13** 3985
- [94] Wu X, Alvarez-Ibarra A, Salahub D and de la Lande A 2018 *Eur. J. Phys. D* **72** 206
- [95] Parise A, Alvarez-Ibarra A, Wu X, Hao X, Pilmè J and de la Lande A 2018 *J. Phys. Chem. Lett.* **9** 844
- [96] Chu X and Memoli P J 2011 *Chem. Phys.* **391** 83
- [97] Ding F, Liang W, Chapman C T, Isborn C M and Li X 2011 *J. Chem. Phys.* **135** 164101
- [98] Runge E and Gross E K U 1984 *Phys. Rev. Lett.* **52** 997
- [99] Gross E K U and Kohn W 1985 *Phys. Rev. Lett.* **55** 2850
- [100] White A, Heide C J, Saalfrank P, Head-Gordon M and Luppi E 2016 *Mol. Phys.* **114** 947
- [101] Sonk J A, Caricato M and Schlegel H B 2011 *J. Phys. Chem. A* **115** 4678
- [102] Sonk J A and Schlegel H B 2011 *J. Phys. Chem. A* **115** 11832–11840
- [103] Perdew J 1979 *Chem. Phys. Lett.* **64** 127–130
- [104] Perdew J and Zunger A 1981 *Phys. Rev. B* **23** 5048–5079
- [105] Vydrov O A and Scuseria G E 2006 *J. Chem. Phys.* **125** 234109
- [106] Vydrov O A, Heyd J, Krukau A V, and Scuseria G E 2006 *J. Chem. Phys.* **125** 074106
- [107] Chai J D and Head-Gordon M 2009 *J. Chem. Phys.* **131** 174105
- [108] Zapata F, Luppi E and Toulouse J 2019 *J. Chem. Phys.* **150** 234104
- [109] van Leeuwen R and Baerends E 1994 *Phys. Rev. A* **49** 2421
- [110] Gauriot N, Vénierard V and Luppi E 2019 *J. Chem. Phys.* **151** 234111
- [111] Pauletti C F, Coccia E and Luppi E 2021 *J. Chem. Phys.* **154** 014101

- [112] Helgaker T, Jorgensen P and Olsen J 2000 *Molecular Electronic-Structure Theory* (John Wiley & Sons Inc)
- [113] Dreuw A and Head-Gordon M 2005 *Chem. Rev.* **105** 4009
- [114] Sato T, Pathak H, Orimo Y and Ishikawa K L 2018 *J. Chem. Phys.* **148** 051101
- [115] Pathak H, Sato T and Ishikawa K L 2020 *J. Chem. Phys.* **152** 124115
- [116] Sato T, Teramura T and Ishikawa K L 2018 *Appl. Sci.* **8** 433
- [117] Gorlach A, Neufeld O, Rivera N, Cohen O and Kammerer I 2020 *Nat. Commun.* **11** 4598
- [118] Marengo E A and Khodja M R 2006 *Phys. Rev. E* **74**(3) 036611 URL <https://link.aps.org/doi/10.1103/PhysRevE.74.036611>
- [119] Wang C M, Ho T S and Chu S I 2016 *Journal of Physics B: Atomic, Molecular and Optical Physics* **49** 225401 URL <https://doi.org/10.1088/0953-4075/49/22/225401>
- [120] Schirmer J 1991 *Phys. Rev. A* **43** 4647
- [121] Schirmer J and Trofimov A B 2004 *J. Chem. Phys.* **120** 11449
- [122] Luppi E and Head-Gordon M 2013 *J. Chem. Phys.* **139** 164121
- [123] Schlegel H B, Smith S M and Li X 2007 *J. Chem. Phys.* **126** 244110
- [124] Coccia E and Luppi E 2019 *Theor. Chem. Acc.* **138** 96
- [125] Luppi E and Coccia E 2021 *Phys. Chem. Chem. Phys.* **23** 3729
- [126] Saalfrank P, Bedurke F, Heide C, Klamroth T, Klinkusch S, Krause P, Nest M and Tremblay J C 2020 *Adv. Quant. Chem.* **81** 15
- [127] Pabst S and Santra R 2014 *J. Phys. B* **47** 124026
- [128] Pabst S and Santra R 2013 *Phys. Rev. Lett.* **111** 233005
- [129] Pabst S, Sytcheva A, Geffert O and Santra R 2016 *Phys. Rev. A* **94**(3) 033421
- [130] Teramura T, Sato T and Ishikawa K L 2019 *Phys. Rev. A* **100** 043402
- [131] McWeeny R 1983 *Int. J. Quant. Chem.* **23** 405
- [132] Moccia R 1974 *Int. J. Quant. Chem.* **8** 293
- [133] Koch O, Kreuzer W and Scrinzi A 2006 *Appl. Math. Comput.* **173** 960
- [134] Haxton D J, Lawler K V and McCurdy C W 2011 *Phys. Rev. A* **83** 063416
- [135] Haxton D J and McCurdy C W 2015 *Phys. Rev. A* **91** 012509
- [136] Wahyutama I S, Sato T and Ishikawa K L 2019 *Phys. Rev. A* **99** 063420
- [137] Miyagi H and Madsen L B 2013 *Phys. Rev. A* **87** 062511
- [138] Miyagi H and Madsen L B 2014 *Phys. Rev. A* **89** 063416
- [139] Pathak H, Sato T and Ishikawa K L 2020 *Mol. Phys.* **118** e1813910
- [140] Ruberti M, Averbukh V and Decleva P 2014 *J. Chem. Phys.* **141** 164126
- [141] Ullrich C A 2011 *Time-Dependent Density-Functional Theory: Concepts and Applications* (OUP Oxford)
- [142] Floss I, Lemell C, Wachter G, Smejkal V, Sato S A, Tong X M, Yabana K and Burgdörfer J 2018 *Phys. Rev. A* **97** 011401(R)
- [143] Elliott P, Goldson S, Canahui C and Maitra N T 2011 *Chem. Phys.* **391** 110
- [144] Raghunathan S and Nest M 2011 *J. Chem. Theory Comput.* **7** 2492
- [145] Elliott P, Fuks J I, Rubio A and Maitra N T 2012 *Phys. Rev. Lett.* **109** 266404
- [146] Provorse M R and Isborn C M 2016 *Int. J. Quantum Chem.* **739** 116
- [147] Hoerner P, Lee M K and Schlegel B 2019 *J. Chem. Phys.* **151** 054201
- [148] Grobas Illobre P, Marsili M, Corni S, Stener M, Toffoli D and Coccia E 2021 *J. Chem. Theory Comput.* Accepted
- [149] Schneider I 1997 *Phys. Rev. A* **55** 3417
- [150] Prauzner-Bechcicki J S, Sacha K, Eckhardt B and Zakrzewski J 2008 *Phys. Rev. A* **78** 013419
- [151] Peng L Y and Starace A F 2006 *J. Chem. Phys.* **125** 154311
- [152] Grum-Grzhimailo A N, Abeln B, Bartschat K, Wefen D and Urness T 2010 *Phys. Rev. A* **81** 043408
- [153] Patchkovskii S and Muller H G 2016 *Comput. Phys. Commun.* **199** 153
- [154] Müller A D, Kutscher E, Artemyev A N, Cederbaum L S and Demekhin P V 2018 *Chem. Phys.* **509** 145
- [155] Ruiz C, Plaja L, Roso L and Becker A 2006 *Phys. Rev. Lett.* **96** 053001
- [156] Ivanov I A and Kheifets A S 2009 *J. Phys. B* **42** 145601
- [157] Parker J S, Moore L R, Dundas D and Taylor K T 2000 *J. Phys. B* **33** L691
- [158] Parker J S, Meharg K J, McKenna G A and Taylor K T 2007 *J. Phys. B* **40** 1729
- [159] Robicheaux F 2012 *J. Phys. B* **45** 135007
- [160] de Boor C 1978 *A practical guide to splines* (Springer-Verlag, NewYork)
- [161] Bachau H, Cormier E, Decleva P, Hansen J E and Martin F 2001 *Rep. Prog. Phys.* **64** 1601
- [162] Toffoli D and Decleva P 2016 *J. Chem. Theory Comput.* **12** 4996
- [163] Kaufmann K, Baumeister W and Jungen M 1989 *J. Phys. B: At. Mol. Opt. Phys.* **22** 2223
- [164] Faure A, Gorfinkiel J, Morgan L A and Tennyson J 2002 *Comput. Phys. Commun.* **144** 224
- [165] Nestmann B M and Peyerimhoff S D 1990 *J. Phys. B* **23** L773
- [166] Fiori M and Miraglia J E 2012 *Comput. Phys. Commun.* **183** 2528
- [167] Woźniak A P, Lesiuk M, Przybytek M, Efimov D K, Prauzner-Bechcicki J S, Mandrysz M, Ciappina M, Pisanty E, Zakrzewski J, Lewenstein M and Moszyński R 2021 *J. Chem. Phys.* **154** 094111
- [168] Bedurke F, Klamroth T, Krause P and Saalfrank P 2019 *J. Chem. Phys.* **150** 234114
- [169] Li X, Smith S M, Markevitch A N, Romanov D A, Levis R J, and Schlegel H B 2005 *Phys. Chem. Chem. Phys.* **7** 233
- [170] Marante C, Argenti L and Martin F 2014 *Phys. Rev. A* **90** 012506
- [171] González-Vázquez J, Klinker M, Marante C, Argenti L, Corral I and Martín F 2015 *J. Phys.: Conf. Ser.* **635** 112110
- [172] Yip L, McCurdy C W and Rescigno T N 2014 *Phys. Rev. A* **90** 063421
- [173] McCurdy Jr C W and Rescigno T N 1978 *Phys. Rev. Lett.* **41** 1364
- [174] McCurdy C W and Mowrey R C 1982 *Phys. Rev. A* **25** 2529
- [175] White A F, Epifanovsky E, McCurdy C W and Head-Gordon M 2017 *J. Chem. Phys.* **146** 234107
- [176] Ammar A, Leclerc A and Ancarani L U 2020 *J. Comput. Chem.* **41** 2365
- [177] Matsuzaki R and Yabushita S 2017 *J. Comput. Chem.* **38** 910
- [178] Matsuzaki R and Yabushita S 2017 *J. Comput. Chem.* **38** 2030
- [179] Matsuzaki R, Asai S, McCurdy C W and Yabushita S 2014 *Theor. Chem. Acc.* **133** 1
- [180] Kosloff R and Kosloff D 1986 *J. Comput. Phys.* **63** 363
- [181] Riss U V and Meyer H D 1996 *J. Chem. Phys.* **105** 1409
- [182] Manolopoulos D E 2002 *J. Chem. Phys.* **117** 9552
- [183] Gonzalez-Lezana T, Rackham E J and Manolopoulos D E 2004 *J. Chem. Phys.* **120** 2247

- [184] Grozdanov T P and McCarrroll R 2007 *J. Chem. Phys.* **126** 034310
- [185] Zuev D, Jagau T C, Bravaya K B, Epifanovsky E, Shao Y, Sundstrom E, Head-Gordon M and Krylov A I 2014 *J. Chem. Phys.* **141** 024102
- [186] Klinkusch S, Saalfrank P and Klamroth T 2009 *J. Chem. Phys.* **131** 114304
- [187] Telnov D A and Chu S I 2007 *Phys. Rev. A* **76** 043412
- [188] Tchitchevokova D S, Lu H, Chelkowski S and Bandrauk A D 2011 *J. Phys. B* **44** 065601
- [189] Bauer J, Plucinski L, Piraux B, Potvlieghe R, Gajda M and Krzywinski J 2001 *J. Phys. B* **34** 2245
- [190] Lein M, Hay N, Velotta R, Marangos J P and Knight P L 2002 *Phys. Rev. A* **66** 023805
- [191] Taïeb R, Veniard V, Wassaf J and Maquet A 2003 *Phys. Rev. A* **68** 033403
- [192] Yuan K J and Bandrauk A D 2019 *Phys. Rev. A* **100** 033420
- [193] Castro A, Rubio A and Gross E K 2015 *Eur. Phys. J. B* **88** 191
- [194] Bandrauk A D, Chelkowski S, Diestler D J, Manz J and Yuan K J 2009 *Phys. Rev. A* **79** 023403
- [195] Avanaki K N, Telnov D A and Chu S I 2014 *Phys. Rev. A* **90** 033425
- [196] Telnov D A, Heslar J and Chu S I 2014 *Phys. Rev. A* **90** 063412
- [197] Telnov D A, Heslar J and Chu S I 2017 *Phys. Rev. A* **95** 043425
- [198] Chu X and Chu S I 2001 *Phys. Rev. A* **63** 023411
- [199] Chu X and Chu S I 2001 *Phys. Rev. A* **64** 063404
- [200] Chu X and Groenenboom G C 2012 *Phys. Rev. A* **85** 053402
- [201] Kato T and Kono H 2004 *Chem. Phys. Lett.* **392** 533
- [202] Li W Y, Xu R H, Xie X J and Chen Y J 2019 *Phys. Rev. A* **100** 043421
- [203] Neufeld O and Cohen O 2020 *Phys. Rev. Res.* **2** 033037
- [204] Romanov A A, Silaev A A, Frolov M V and Vvedenskii N V 2020 *Phys. Rev. A* **101** 013435
- [205] Ganeev R A, Witting T, Hutchison C, Frank F, Tudorovskaya M, Lein M, Okell W A, Zair A, Marangos J P and Tisch J W G 2012 *Opt. Express* **20** 25239
- [206] Minemoto S, Umegaki T, Oguchi Y, Morishita T, ans S Watanabe A T L and Sakai H 2008 *Phys. Rev. A* **78** 061402(R)
- [207] Wörner H J, Niikura H, Bertrand J B, Corkum P B and Villeneuve D 2009 *Phys. Rev. Lett.* **102** 103901
- [208] Higuete J, Ruf H, Thiré N, Cireasa R, Constant E, Cormier E, Descamps D, Mével E, Petit S, Pons B, Mairesse Y and Fabre B 2011 *Phys. Rev. A* **83** 053401
- [209] Tong X M and Chu S I 2001 *Phys. Rev. A* **64** 013417
- [210] Telnov D A and Chu S I 2009 *Phys. Rev. A* **80** 043412
- [211] Heslar J, Telnov D and Chu S I 2011 *Phys. Rev. A* **83** 043414
- [212] Dundas D 2012 *J. Chem. Phys.* **136** 194303
- [213] Chu X and Groenenboom G C 2013 *Phys. Rev. A* **87** 013434
- [214] Chu X and Groenenboom G C 2016 *Phys. Rev. A* **93** 013422
- [215] Fowe E P and Bandrauk A D 2010 *Phys. Rev. A* **81** 023411
- [216] Mauger F, Abanador P M, Scarborough T D, Gorman T T, Agostini P, DiMauro L F, Lopata K, Schafer K J and Gaarde M B 2019 *Struct. Dynam.* **6** 044101
- [217] Gorman T T, Scarborough T D, Abanador i P M, Mauger F, Kiesewetter D, Sándor P, Khatri S, Lopata K, Schafer K J, Agostini P, Gaarde M B and DiMauro L F 2019 *J. Chem. Phys.* **150** 184308
- [218] Fowe E P and Bandrauk A D 2011 *Phys. Rev. A* **84** 035402
- [219] Mulholland P and Dundas D 2018 *Phys. Rev. A* **97** 043428
- [220] Monfared M, Irani E and Sadighi-Bonabi R 2018 *J. Chem. Phys.* **148** 234303
- [221] Irani E and Monfared M 2019 *Chem. Phys. Lett.* **719** 27
- [222] Wardlow A and Dundas D 2016 *Phys. Rev. A* **93** 023428
- [223] Zhou S, Li Q, Guo F, Wang J, Chen J and Yang Y 2021 *Chem. Phys.* **545** 111147
- [224] Farrell J, McFarland B, Gühr M and Bucksbaum P 2009 *Chem. Phys.* **366** 15
- [225] Vozzi C, Calegari F, Benedetti E, Caumes J P, Sansone G, Stagira S and Nisoli M 2005 *Phys. Rev. Lett.* **95** 153902
- [226] Yun H, Lee K M, Sung J H, Kim K T, Kim H T and Nam C H 2015 *Phys. Rev. Lett.* **114** 153901
- [227] Hutchison C, Ganeev R, Castillejo M, Lopez-Quintas I, Zair A, Weber S, McGrath F, Abdelrahman Z, Oppermann M, Martin M, Lei D, Maier S, Tisch J and Marangos J 2013 *Phys. Chem. Chem. Phys.* **15** 12308–12313
- [228] Zhu X, Liu X, Lan P, Wang D, Zhang Q, Li W and Lu P 2016 *Opt. Express* **24** 24824
- [229] Liu X, Li P, Zhu X, Lan P, Zhang Q and Lu P 2017 *Phys. Rev. A* **95** 033421
- [230] Kaneshima K, Ninota Y and Sekikawa T 2018 *Opt. Express* **26** 31039
- [231] Wilson B P, Fulfer K D, Mondal S, Ren X, Tross J, Poliakov E D, Jose A T L, Lucchese R R and Trallero-Herrero C 2016 *J. Chem. Phys.* **145** 224305
- [232] Heyl C M, Arnold C L, Couairon A and L’Huillier A 2017 *J. Phys. B* **50** 013001
- [233] Jin C, Le A T and Lin C D 2011 *Phys. Rev. A* **83** 023411
- [234] Li P C and Chu S I 2013 *Phys. Rev. A* **88** 053415
- [235] Joyce T and Jaron-Becker A 2020 *Opt. Lett.* **45** 1954
- [236] Foulkes W M C, Mitas L, Needs R J and Rajagopal G 2001 *Rev. Mod. Phys.* **73** 33
- [237] Austin B M, Zubarev D Y and Lester Jr W A 2012 *Chem. Rev.* **112** 263
- [238] Scemama A, Caffarel M, Oseret E and Jalby W 2013 *QMC=Chem: A Quantum Monte Carlo Program for Large-Scale Simulations in Chemistry at the Petascale Level and beyond* vol 7851 (Springer, Berlin, Heidelberg)
- [239] Mussard B, Coccia E, Assaraf R, Otten M, Umrigar C J and Toulouse J 2018 *Adv. Quant. Chem.* **76** 255
- [240] Kim J, Baczewski A D, Beaudet T D, Benali A, Bennett M C, Berrill M A, Blunt N S, Landinez Borda E J, Casula M, Ceperley D M, Chiesa S, Clark B K, Clay III R C, Delaney K T, Dewing M, Esler K P, Hao H, Heinonen O, Kent P R C, Krogel J T, Kylänpää I, Li Y W, Lopez M G, Luo Y, Malone F D, Martin R M, Amrita Mathuriya and J M, Melton C A, Mitas L, Morales M A, Neuscamm E, Parker W D, Pineda Flores S D, Romero N A, Rubenstein B M, Shea J A R, Shin H, Shulenburg L, Tillack A F, Townsend J P, Tubman N M, Van Der Goetz B, Vincent J E, Yang D C, Yang Y, Zhang S and Zhao L 2018 *J. Phys. Condens. Matter* **30** 195901
- [241] Nakano K, Attaccalite C, Barborini M, Capriotti L, Casula M, Coccia E, Dagrada M, Genovese C, Luo Y, Mazzola G, Zen A and Sorella S 2020 *J. Chem. Phys.* **152** 204121